ANTIBODY-FUNCTIONALIZED CARBON NANOTUBES IN CANCER THERAPY

Submitted to: Dr. Bagajewicz, Professor
University of Oklahoma

Submitted by: Kyung Kim
Kristina Tran
University of Oklahoma

May 2, 2008

TABLE OF CONTENTS

LIST OF FIGURES

LIST OF TABLES

1. Abstract

As breast cancer is the second leading cancer in women today with a projected 1.6 million victims in the US, we want to develop a treatment to attach monoclonal antibodies to single-walled carbon nanotubes (SWNT) to selectively target breast cancer cells and then use near-infrared (NIR) radiation to eradicate the tumors.

Carbon nanotubes were selected as the delivery vehicle due to its small size and unique properties (most notably, its strong adsorption of NIR). This treatment has already shown success on the laboratory scale. As a minimally invasive alternative to traditional breast cancer treatments, such as chemotherapy or surgery, this treatment offers increased cancer cell death and minimal side effects to normal tissues.

The proposed treatment administration is based largely on mathematical models that predict the initial dosage for intravenous injection, emitting time for the NIR radiation as a function of the tumor volume. Tissue disposition of the drug was also modeled based on the Physiologically-based pharmacokinetics (PBPK) model; this indicates the optimal time to begin irradiation – when the drug concentration in the surrounding cells is at a minimum. The total amount of SWNTs was calculated to 8.01E-11 moles by using random number generation. Additionally, we have developed a model that predicts the required time for tumor damage and temperature gradient during NIR irradiation. Based on the temperature gradients, the optimal length of irradiation is three minutes.

The large-scale production of the drug treatment includes cultivation of the monoclonal antibodies, as well as their conjugation to the SWNTs. The total capital investment was estimated to be $128 million. The total product cost for the drug is $760 per gram.

By using mathematical models, we are providing the laboratory-tested cancer therapy a means to be more useful at the clinical level by considering the individuality of the patient.

2. Introduction

Over a quarter of a million women suffer from breast cancer in the US. In order to address the problems of current breast cancer treatment and to improve the quality of life for patients, an exploration of novel cancer treatments is done.

The subject of nanomedicine is one that has high promise. From clinical diagnoses to drug delivery, the use of nanotechnology in medical applications offers new ways to improve human health at the molecular level. Nanoparticles are known to have a large surface area per unit mass, which increases biological activity[5]. In the field of cancer therapy, the use of nano-sized delivery systems to selectively target tumors is one that is widely researched. Some advantages to using nanostructures in drug delivery and cancer therapy are the following[41]:

- They can penetrate barriers that are difficult in conventional drug delivery
- They can deliver a drug treatment directly to the cells.
- They can penetrate tumors due to the "leaky" nature of the tumor vasculature

One delivery system of interest to researchers is the use of single-walled carbon nanotubes. When conjugated with monoclonal antibodies, the carbon nanotubes are allowed to reach the cancer site. After irradiation with a near-infrared laser, localized heating occurs, and cancer cells can be destroyed.

2.1 Monoclonal Antibodies

When foreign molecules, also known as antigens, enter the body, they are recognized by the immune system. Globular proteins found in serum or body secretions are called antibodies; these Y-shaped proteins react with antigens to neutralize or destroy them. Antibodies are produced by B lymphocyte cells. Those produced from a single B lymphocyte and are of only one specificity are termed monoclonal antibodies (mAb)[4].

Monoclonal antibodies are very important in medicine, especial in the treatment of human cancer. Cancerous cells contain surface antigens not expressed on normal cells. Monoclonal antibodies, because of their specificity, are able to distinguish between normal and cancer cells. Thus they can serve as a medium for delivering toxins directly to the desired site[4].

Because the breast cancer cells have an overexpression of the HER2 and IGF1R receptors, it is desirable to use monoclonal antibodies that target those receptors.

Figure 1 shows monoclonal antibodies (the yellow, Y-shaped proteins) binding to the breast cancer receptor HERS (in purple).

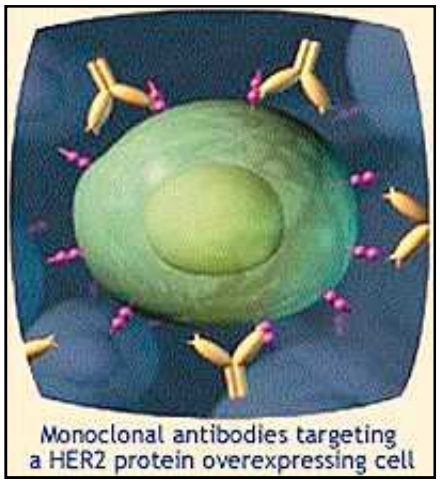

Figure 1: Monoclonal antibodies targeting a breast cancer cell

3. Breast Cancer

As defined by the American Cancer Society, cancer "is characterized by uncontrolled growth and spread of cancer cells[1]." It is the second leading cause of US mortality, killing over half a million people in 2003[2]. Over 270,000 US women are diagnosed with breast cancer, and it was estimated that 40,000 will die[2-3].

The breast tissue is made of milk production glands called lobules and the ducts that join the lobules to the nipple. The rest of the breast is comprised of fatty and lymphatic tissue. Most breast cancer tumors (a lump of cancerous cells) are invasive, starting in the lobules or ducts of

and spreading to the surrounding breast tissue. The severity of breast cancer is categorized into five stages, with Stage IV being the most advanced[3]. Table 1 below summarizes the stages of breast cancer development:

Stage	Definition
Stage 0	Cancer cells remain inside the breast duct, without invasion into normal adjacent breast tissue
Stage I	Cancer is 2 cm or less and is confined to the breast (lymph nodes are clear)
Stage II	The tumor is over 2 cm but no larger than 5 cm Or There is spread to the lymph nodes under the arm
Stage III	Also called locally-advanced cancer. The tumor is more than 5 cm across The cancer is extensive in the underarm lymph nodes It has spread to other lymph nodes or tissues near the breast
Stage IV	The cancer has spread—or metastasized—to other parts of the body.

Table 1: Stages of Breast Cancer Development

Source: *breastcancer.org, http://www.breastcancer.org/about_us/press_room/press_kit/cancer_facts.jsp#nci*

Breast cancer at the early stage usually has no symptoms since the tumor is small and easily treatable. As the cancer advances, the most common symptom is a lump in the breast. The detection of breast cancer can be done through mammography, magnetic resonance imaging (MRI), clinical breast examination, or through self-exams[3].

3.1 Existing Breast Cancer Treatments

Treatment for breast cancer is decided based on several factors, including the cancer stage, age of the patient, preference of the patient, and health risks. The most common type of treatment is surgery, which is often combined with other treatments like hormonal therapy, chemotherapy, and radiation therapy[3].

Surgery involves removing the cancerous tissue. Lumpectomy is the removal of cancerous tissue in addition to a small rim of normal tissue. Mastectomy is the removal of the entire breast. Surgery is not always convenient and sometimes also calls for breast reconstruction of mastectomy is done[3].

Chemotherapy involves the release of drugs into the body that kill cancer cells. Adjuvant chemotherapy is usually done after the patient's surgery to increase the chances of her survival.

Common drugs used in chemotherapy include cyclophosphamide, methotrexate, doxorubicin, paclitaxal, and docetaxel[3]. For women with large tumors and a high risk of cancer recurrence, chemotherapy significantly increases her survival. However, the side effects of chemotherapy need to be taken into consideration before treatment decision is made. Table 2 lists the short-term and long-term side effects of chemotherapy[17].

Short-term Effects	Long-term Effects
Emesis	Premature menopause
Nausea	Infertility
Stomatitis	Weight gain
Alopecia	Cardiac dysfunction
Myelosuppression	Leukemia
Thromboembolism	Myelodyspastic syndrome
Myalgias	Cognitive dysfunction
Neuropathy	
Fatigue	

Table 2: Side Effects of Chemotherapy

Source: Partridge, A. et al., Side effects of chemotherapy and combined chemohormonal therapy in women with early-stage breast cancer, *Journal of the National Cancer Institute Monographs*, 30:135-142.

The most common side effects of chemotherapy are nausea, alopecia (hair loss), premature menopause, and weight gain[17].

In radiation therapy following surgery, cancer cells are destroyed pre-surgery or post-surgery. External radiation therapy uses a machine to target the affected area from outside the body. In internal radiation therapy or brachytherapy, a radioactively-filled seed or needle is inserted near the cancer site[3]. Some side effects of radiation therapy are the damage to normal tissue[18], cytotoxicity to cells[18], nausea[19], fatigue[19], and leucopenia[19].

3.2 Alternative Breast Cancer Treatments

Trastuzumab, a humanized monoclonal antibody, has become influential in treating metastatic breast cancer. This drug is injected intravenously and targets the HER2 receptors expressed on the breast cancer cells[20]. The results have been significant; a three-year study reported the disease-free survival of 87% compared to a control group[21]. The side effects associated with chemotherapy – leucopenia, thrombocytopenia, and alopecia – are rare under TrastuzumAb[20].

Unfortunately, this drug comes with a risk of cardiac side effects. Congestive heart failure was seen in 27% of the women who received trastuzumab and doxorubicin and in 13% of the women who received trastuzumab and paclitaxel. The mechanism of cardiac toxicity with trastuzumab is not yet elucidated[21].

4. Carbon Nanotubes

Since its first discovery in 1975, carbon nanotubes have stretched the limits of nanoscience. They have been extensively studied during the past two decades. Carbon nanotubes, due to their unique properties, offer promise in many applications, including electronics, novel materials, and medicine. The two main types of existing carbon nanotubes are single-walled carbon nanotubes (SWNT) and multi-walled carbon nanotubes (MWNT), whose main difference is the number of concentric graphite layers[5]. For this report, we will be concerned with SWNTs due to its relative simplicity compared to MWNTs.

The structure of carbon nanotubes consists of a graphite sheet rolled into a cylinder that may be capped at the ends (Figure 2). The diameter of SWNTs range from .4 to 2 nm, and the length can be up to several micrometers[5].

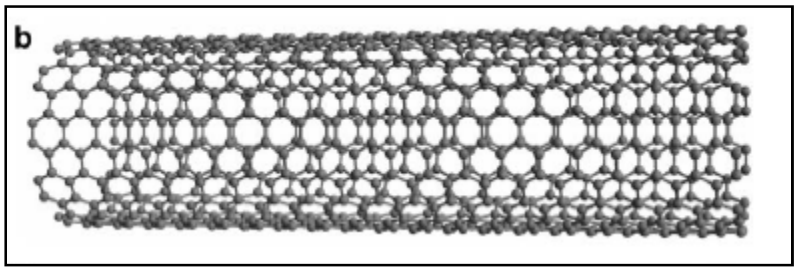

Figure 2: Diagram of a single-walled carbon nanotube

Source: *Britz, D. and Khlobystov, A., Noncovalent interactions of molecules with single walled carbon nanotubes, Chemical Society Reviews (2006), 35:637-659.*

3.1 Properties of Carbon Nanotubes

SWNTs can behave as either metals or semiconductors, depending on its diameter and how it wraps. They can be used to form junctions between crossed nanotubes and can act as diodes or rectifiers. Thus, circuitry based on SWNTs is possible. Carbon-carbon bonds in SWNTs make up the strongest chemical bonds in nature. The Young's modulus of carbon nanotubes, a measure of stiffness, was determined to be larger than most materials. Experiments have also revealed the resilient nature of SWNTs; its yield point is at extreme temperature and loads. The high thermal conductivity and ability to absorb radiation, as seen later, can be exploited for nanomedical applications[6]. Further research and characterization of these nanomaterials will lead to more efficient and newer applications.

3.2 Carbon Nanotubes in Drug Delivery

The development of drug delivery systems is important for improving therapeutic properties of drugs administered to the human body. Standard therapeutic treatments are associated with non-specific biodistribution and rapid metabolism of the drug before reaching its target[7]. Due to its small size and ease of cellular uptake, SWNTs are being studied as vectors for drug delivery[5].

The mechanism of cellular internalization of SWNTs is not yet fully elucidated. One postulation is that carbon nanotubes enter the cells through the plasma membrane and undergo passive diffusion across the lipid bilayer. Experimental observations suggest that the SWNTs are

positioned perpendicularly to the plasma membrane and penetrate similar to “nanoneedles” [7]. An alternative route to internalization is endocytosis[7]. Endocytosis is the process whereby cells engulf other molecules with their membrane[5]. Figure 3 shows an example of cellular uptake by endocytosis.

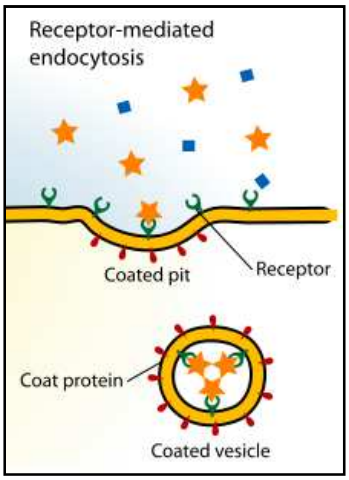

Figure 3: Receptor-mediated endocytosis

When molecules bind to the receptors along the outside of a cell membrane, the membrane pinches inward and encapsulates the molecules as they become internalized[7].

Their ability to adsorb near-infrared radiation makes SWNTs a viable component in cancer therapy. Recent research has demonstrated that by using a laser wavelength of 808 nm, the localized heating due to the high thermal conductivity of SWNTs led to successful eradication of the cancer cells[8]. SWNTs and their role in photothermal therapy will be discussed later.

3.3 Biomolecule Attachment to Carbon Nanotubes

The modification of carbon nanotube surfaces improves pharmacokinetic and solubility properties, thus making them more appealing for use as drug delivery systems[7]. Molecules that have been attached to SWNT include nucleic acids, peptides, polymers, oligomers, surfactants, antibodies, and other proteins. Surfactants are often used to disperse SWNTs in solution. This is desirable in order to prevent agglomeration of SWNTs, which increases toxicity and limits

functionality. Functionalized SWNTs provide aqueous solubility and decreased toxicity[5]. Three modes of attachment have been studied by researchers: encapsulation[9], covalent functionalization, and noncovalent functionalization.

The small diameters and long length of the SWNTs enable the encapsulation of molecules inside the tube (Figure 4). Spontaneous crossing of the SWNT barrier can be done as long as the molecule is smaller than the nanotube diameter and as long as the surface tension of the liquid solution is below 200 nM/m[9]. One of the most difficult aspects of this method is retaining the smaller molecules inside of the SWNT.

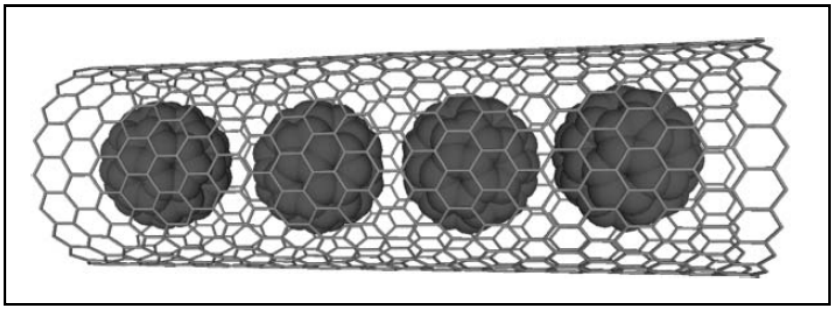

Figure 4: Encapsulation of a molecule

Source: *Britz, D. and Khlobystov, A., Noncovalent interactions of molecules with single walled carbon nanotubes, Chemical Society Reviews (2006), 35:637-659.*

Covalent modification of SWNTs is done through addition reactions (Figure 5). As the name suggests, the molecules are held to the surface walls through covalent bonds. SWNTs undergo oxidative treatment using strong acid solutions. Another method of covalent attachment is based on addition reactions to the SWNT[5]. Adding covalent functionality to the SWNT permanently disrupts the structure and alters the electronic properties[7].

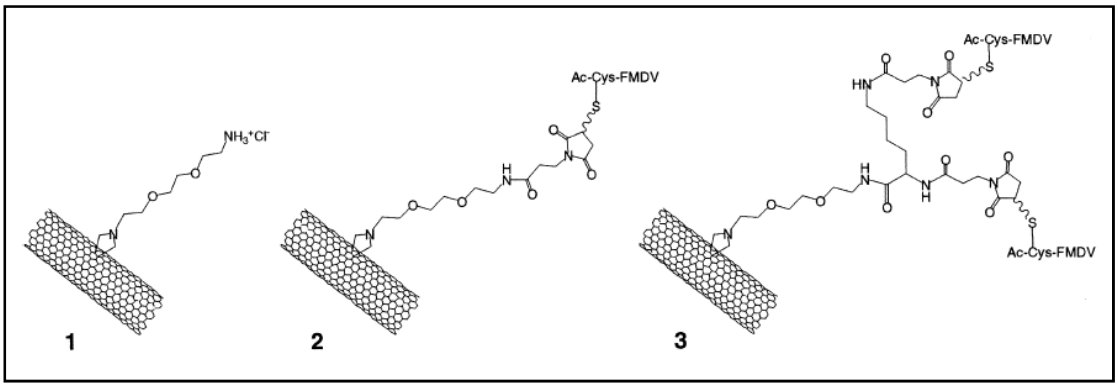

Figure 5: An amino-derivatized carbon nanotube covalently linked to a peptide

Source: *Pantarotto et. al, Immunization with peptide-functionalized carbon nanotubes enhances virus-specific neutralizing antibody responses, Chemistry & Biology, Vol. 10 (2003).*

To overcome the weaknesses of covalent functionalization, noncovalent interactions should be considered (Figure 6). Linked through hydrophobic or pi-pi interactions, these weaker noncovalent bonds allow for preservation of the SWNT structure and its unique properties[5].

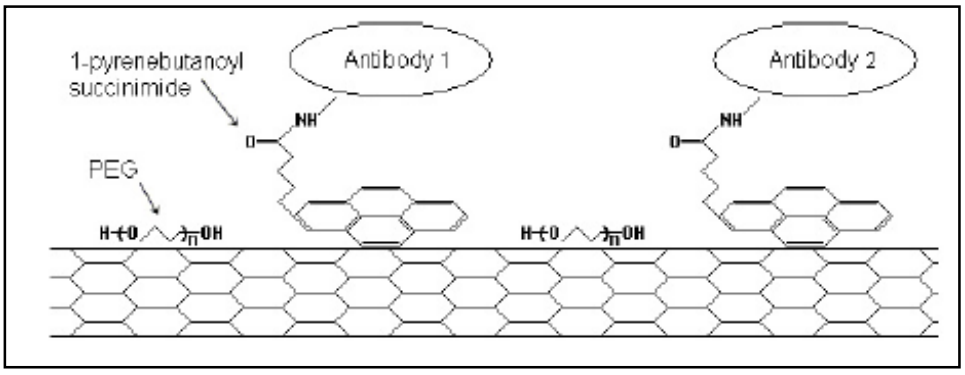

Figure 6: Noncovalent functionalization of 1-pyrenebutanoyl succinimide on a SWNT

Source: *Shao, N. et al., Integrated molecular targeting of IGF1T and HER2 surface receptors and destruction of breast cancer cells using single wall carbon nanotubes, Nanotechnology (2007), 18:1-9.*

The mechanism of mAb-SWNT conjugation is through noncovalent functionalization as shown above. The 1-pyrenebutanoyl succinimide is a linker molecule that binds to the mAb and adsorbs to the surface of the SWNT through pi-pi bonds. The mAb is attached to the linker molecule via amide bonds. The Poly(ethylene glycol) (PEG) is the surfactant that forms a monolayer around the SWNT to prevent other molecules from binding to it.

3.4 Health Effects of Carbon Nanotubes

The cytotoxicity of SWNTs is an important issue that needs to be addressed, especially if they are to be used in medicine. Toxicity was observed in the pulmonary system where pristine SWNT aggregates caused inflammation[10]. Because of their insolubility, these non-functionalized SWNTs agglomerated and resulted in toxic effects when introduced. Thus, it is important to have the walls of SWNTs functionalized, well-dispersed, and water-soluble in order to reduce cytotoxicity[5]. Studies in vitro have demonstrated significantly reduced toxicity from functionalized SWNTs[11]. The toxicology of SWNT is still being researched and is dependent on several parameters, such as nanotube type, nanotube length, type of functionalization, and conjugated molecule[5].

3.5 Biodistribution of Carbon Nanotubes

Research over the pharmacological profile of functionalized carbon nanotubes is lacking today. Knowledge of the pharmacological parameters such as blood circulation, half-life clearance, and tissue biodistribution is essential for intravenous administration. So far only one paper was found concerning the in vivo capabilities of SWNT[12].

Singh, Pantarotto, and colleagues found that the animals displayed no signs of post-administration acute toxicity or mortality. Urine samples showed high presence of intact carbon nanotubes, indicating that the SWNTs were cleared from the blood through renal excretion. Additionally, the functionalized SWNTs used in the study exhibited a half life of 3-3½ hours. Because no other pharmacological literature exists for SWNTs functionalized with monoclonal antibodies, the behaviors of the functionalized SWNTs from this paper were assumed to hold true for the mathematical models and scale-up that will be discussed later[12].

5. Tumor Angiogenesis

It is very crucial to understand how the tumors can be developed. The solid tumors are formed as the many cancerous cells are stacked and attached together. There are three main components in tumors: the cancer cells, which are comprises more than 50% of the tumors; the blood vessels, which are about 1~10%; and the rest of the tumors are composed of a collagen-rich-matrix, called the interstitim[28]. The interstitium is the connective tissue matrix that is used as the permeable cell junction for the transfer of big molecules.

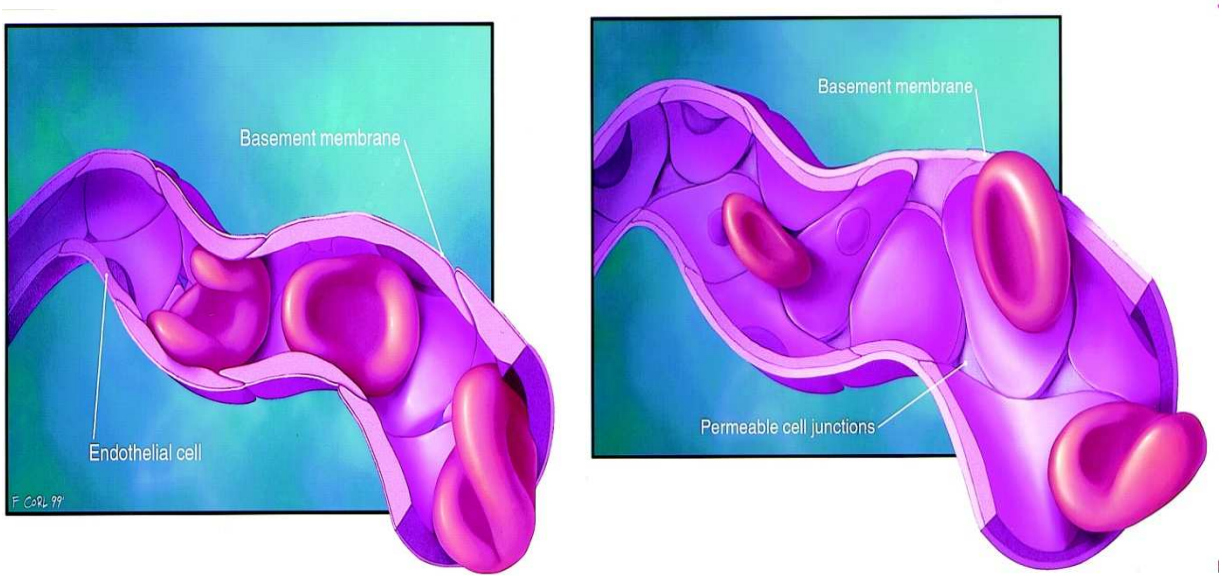

Figure 7: Normal blood vessels before the tumor was invaded (Left). The tumor cells give a signal to the blood vessels to induce the growth of the interstitium (Right) (Kuszyk, et al. 2001).

The tumor cells have to expand the vascular system as the size of cells is increased. The tumor cells would suffocate if there is not enough oxygen and nutrient transfer into the cells. In order for the tumors to survive, the growth of the interstitium is developed by receiving the growth signal from the tumor cells to develop the angiogenesis. This process is as similar as the wound healing. The positive feedback is continually induced until the barrier of the interstitium is broken. In Figure 8, fibrins are erupted into the blood vessels. Fibrin is usually emitted when the wound healing is processed. Fibrin polymers are continually developed and another blood vessels are developed (Figure 9). The tumor blood vessels are tortuous and irregularly shaped

due to the uneven growth. The development tumor angiogenesis can be used as another stepping stone of the process of metastasis. The 'leaky' channels provide more opportunities to spread the tumor cells throughout the whole body system.

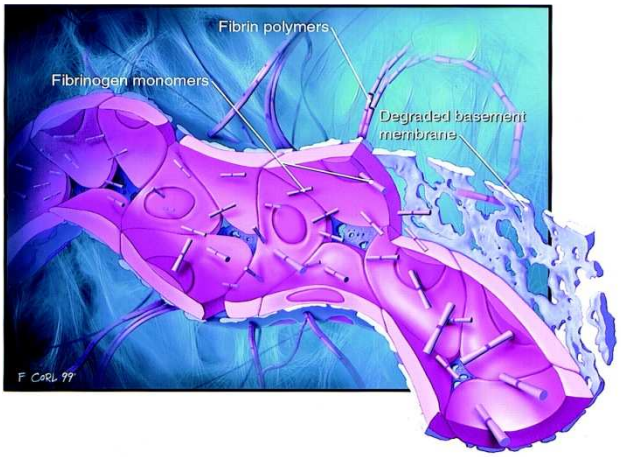

Figure 8: The eruption of the interstitium as the angiogenesis is developed

Figure 9: More vessels are formed after the tumor angiogenesis (Kuszyk, et al. 2001)

5.1 Molecular Transport

There are two methods used to transport the molecules across from the blood vessel: convection and diffusion[29]. The size of monoclonal antibodies is big compared to other cells; the diffusion rate is very slow due to the physiochemical properties. Convection occurs due to the pressure gradient. The driving force of transport the molecules is mainly determined by those two mechanisms. This driving force enables transport of monoclonal antibodies from the blood to the interstitium or the interstitial space to the blood through the lymphatic system[29].

After the monoclonal antibodies reach the receptors, their cellular uptake occurs through phagocytosis and the receptor-mediated endocytosis[29].

5.2 Overcoming Biological Barriers

There are three major barriers that need to be overcome in order for the antibodies to reach the tumors: 1) transport of molecule via blood to tumor, 2) crossing the vessel wall, and 3) crossing the interstitium to the targeted cancer cells. Since the tumor cells are “leaky,” it is not easy to generate enough pressure gradients to transport the antibodies to the tumor. The molecular size of monoclonal antibodies is also an issue when the crossing the vessel wall. The speed of transport is only dependent on diffusion since the pressure gradient is very small[29].

The best way to overcome those barriers is by injecting the antibody into the tumors directly. The method of imaging-guided method to find the position of the tumors is desired where the injection should be performed. However, the residence time of drugs using direct injection inside of tumor cells is short compared to the intravenous injection. One possible reason is that there exists a concentration gradient from the inside of the tumors to the outside of the tumor cells. Hence the conventional method of intravenous injection is desired.

6. Proposed Treatment with Monoclonal Antibodies and Carbon Nanotubes

The following sections will detail how the MAb-SWNT conjugate will be administered. Mathematical models were employed in an attempt to predict the behavior of the treatment and to quantify the dosage required for irradiation with a near-infrared laser.

6.1 Targeting Breast Cancer Receptors

Insulin-like growth factor 1receptor (IGF1R) functions to regulate the cell growth. Though IGF1Rs are also expressed on normal cells, they are overexpressed on 43.8% of breast tumors[31]. Human MCF7 ER+ breast cancer cells demonstrate higher expression of IGF1R as BT474 ER- cancer cells show higher expression of HER2[8]. It is important to know the ratio of the expression of IGF1R and HER2 between normal cells and the breast tumor cancer cells since IGF1R is also expressed on the normal cells.

Human MCF7:IGF1R+ breast cancer cells express 1×10^6 IGF1R/cell[31]. The IGF1R is overexpressed up to 14-fold in ER+ breast cancer cells[32] compared to the normal breast cells whereas very low levels of IGF1R are found in benign breast cancer cells[33]. If one breast cancer cell has 1×10^6 IGF1R receptors, then it is assumed that the overexpression ratio is 14 fold, thus, the percentage of internalized SWNTs in the normal breast cells is calculated by

$$\frac{\#\ of\ IGF1R\ in\ normal\ cell}{\#\ of\ IGF1R\ in\ cancer\ cell} = \frac{1\times10^6\times\frac{1}{14}}{1\times10^6}\times100 = 7.14\ \%$$

The calculation shows that there is a 7.14% chance that normal breast cells could internalize SWNTs. However, the chance of heating up the SWNTs inside of the normal cells by NIR can be minimized by emitting NIR only to the tumors.

Human epidermal growth factor receptor 2 (HER2) tyrosine kinase is another kind of receptor that controls the growth signals, division, and repairs. HER2 is also highly expressed on the

cancer cells – overexpressed about 25% of the breast cancer cells[34]. It is reported that HER2 is overexpressed up to a 25-fold increase in the tumors. The number of receptors in the tumor cells is approximately between 500,000 and 2 million, whereas normal cells only have 20,000 receptors per cell[35]. The percentage of the SWNTs that could be internalized into the normal breast cells based on the number of receptors can be calculated by

$$\frac{\#\ of\ HER2\ in\ normal\ cell}{\#\ of\ HER2\ in\ cancer\ cell} = \frac{20{,}000}{500{,}000 \sim 2{,}000{,}000} \times 100 = 1 \sim 4\ \%$$

The percentage of internalization of SWNTs into normal breast cells is 1-4%. However, as mentioned above, the chance of heating up SWNTs in the normal cells by NIR can be decreased when the NIR is emitted only to the tumor cells.

6.2 Drug Supply into the Tumor Cells via Intravenous Injection

Whole-body distribution study is important to predict the distribution of the concentration of the antibodies through the human body system. Intravenous injection is commonly used to inject the drugs when cancers are treated. As mentioned in the earlier section of tumor angiogenesis, direct injection may overcome the barriers. The antibodies have to cross over the vascular system, the vessel wall, and the interstitium to reach into the cancer tumors. However, the residence time of drugs using direct injection inside of the tumor cells is short compared to intravenous injection. The drugs are easily diffused out of the cancer cells when the direct injection is presented due to the concentration difference of the drugs between the inside of the tumor cells and the interstitium. In other words, a larger amount of initial injection is required to treat cancers, resulting in lower efficiency. Imaging-guided, minimally invasive approaches are desired when the intravenous injection is performed.

6.3 Building a Kinetics Model

The development of a mathematical model is attempted in order to describe the distribution of the concentration of the antibodies in the body. Simulating the monoclonal antibodies for a cancer therapy model is required to find the optimal concentration and the time interval

between the injection of the drugs and emission of the near-infrared laser. Our product would not be favorable by both patients and doctors if the treatment is not convenient and efficient within a reasonable price.

The mathematical model is a nonlinear compartmental system with a tumor compartment[22]. It is described as a function of time after the treatment administration. The binding kinetics is used as described in Figure 8.

$$A + B \rightleftharpoons_{k_b}^{k_a} AB \qquad \textbf{Equation 1}$$

where A is the concentration of substance in the compartment A, B is the concentration of free binding sites in compartment B, and AB is the concentration of bound substance in compartment AB. k_a ,and k_b are the association and dissociation rate constants, respectively.

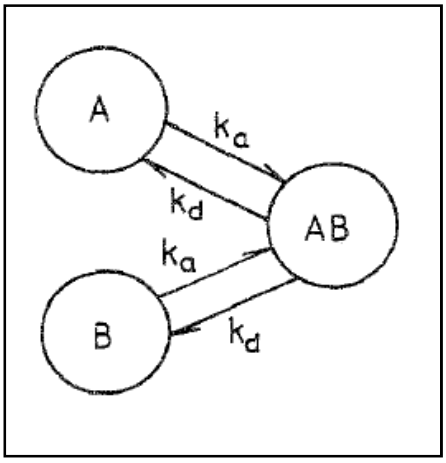

Figure 10: Compartmental model of the elementary binding reaction (Gillian D. Thomas, 1989)

The affinity of the binding reaction is defined as

$$K_{eq} = \frac{k_a}{k_d} \qquad \textbf{Equation 2}$$

The affinity of the binding reaction explains how desirable the substance would be bounded on the receptors. Figure 10 can be described as the set of simultaneous nonlinear ordinary differential equations followed by[23].

$$\frac{d[AB]}{dt} = k_a[A][B] - k_d[AB] \qquad \textbf{Equation 3}$$

$$\frac{d[A]}{dt} = k_d[AB] - k_a[A][B] \qquad \textbf{Equation 4}$$

The total concentration can be expressed based on the law of conservation

Equation 5

where P is the total concentration of possible binding sites at the receptor compartment between the free binding sites and the bound substances. Equations 3 and 4 can be expressed without the component [B] by substituting Equation 5.

$$\frac{d[AB]}{dt} = k_a[A](P - [AB]) - k_d[AB] \qquad \textbf{Equation 6}$$

$$\frac{d[A]}{dt} = k_d[AB] - k_a[A](P - [AB]) \qquad \textbf{Equation 7}$$

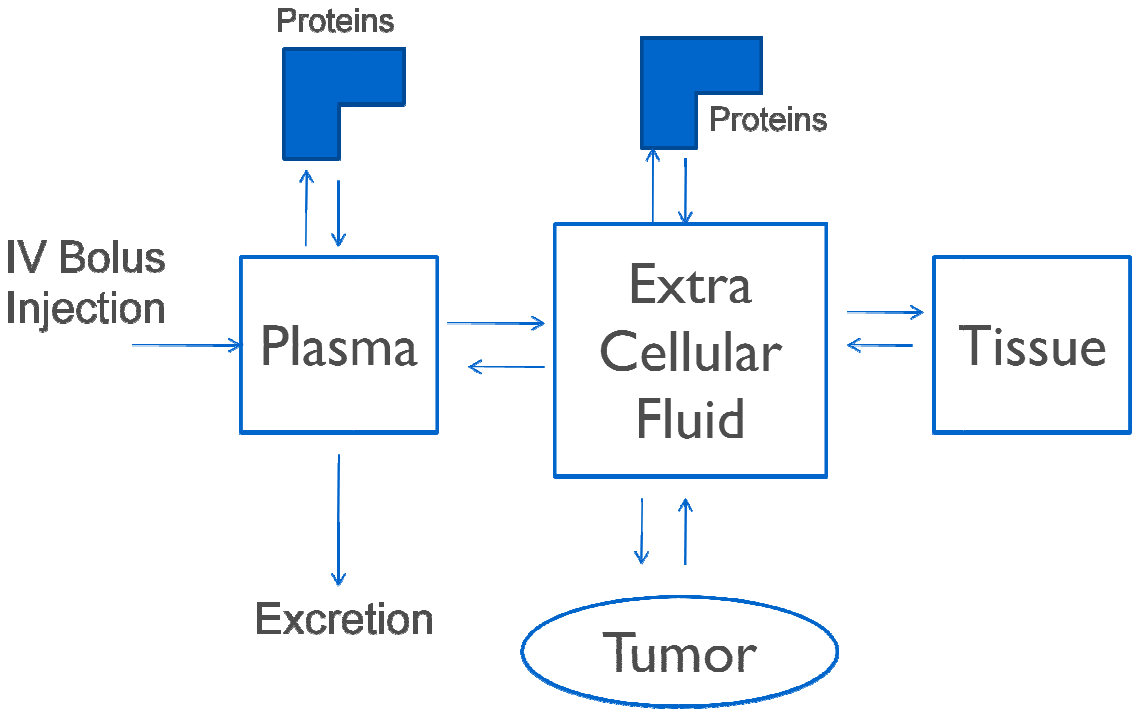

Figure 11: The simplified model of the human body system

Figure 11 depicts a simplified model of the human body. The model has two main compartments: plasma and extracellular fluid (ECF)[22]. The initial dose is introduced directly into the plasma through intravenous bolus injection. The dose in the plasma is diffused through the kidneys, other proteins, tissues, extracellular fluid, and eventually into the tumor cells. The drugs enter the bound compartment from the free sites of the dissociation compartment. Detailed calculations with the parameters, variables, and differential equations are explained in Appendix B.

6.3 Physiologically-based Pharmacokinetic (PBPK) Model

A weakness when the binding kinetics model for the body simulation is that the body system is one big CSTR. The plasma and the extracellular fluid are circulated through the pumping of the heart since the blood circulation system is the closed system. Not only does the binding kinetics need to be addressed in the model, but also the physiological kinetics. In order to explain the body circulation system more reasonably, physiologically based model needs to be developed in order to predict the concentration of mAb in the patient's body.

Physiologically-based pharmacokinetic (PBPK) model is the mathematical model used to describe the physiological phenomena and includes physiological parameters. These parameters include the blood flow rates, lymph flow rates, organ volumes, binding specificity of mAb into the tumors, and metabolisms of drugs[39]. Where simplified pharmacokinetics and pharmacodynamics were inadequate to explain the complex behavior of the body, the PBPK can give a more accurate prediction of the concentration of mAb.

In order to use the PBPK model, there are several characteristics that need to be determined

1. Blood circulation and lymph stream are the major transportation of mAb in body
2. The mAbs diffuse through the capillary blood walls by diffusion and convection
3. Specific binding of the mAb to tumor

4. The antigen is not found in the blood or in any other tissues except the tumor
5. Binding of the antibody to the FcRn receptor in liver, skin and muscle endothelium
6. Catabolic clearance
7. Elimination of catabolic products in kidney by urine.

Figure 12 shows the schematic diagram of the whole body PBPK model. The eight compartments of organs and tissues are further subdivided into the subcompartments, which are the vascular space and interstitial space. The solid lines represent the blood flow stream and the dotted lines are the lymph flow stream. Mass balance equations are used to simulate the PBPK model (See the Appendix C for more detail).

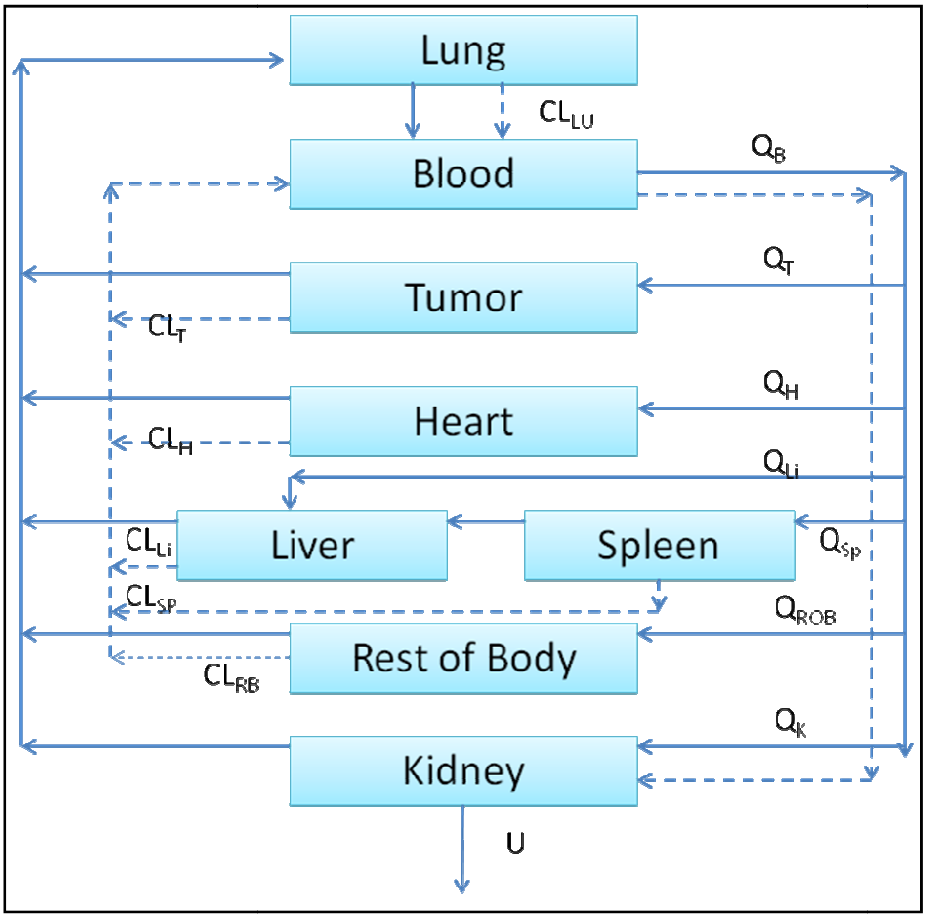

Figure 12: Schematic diagram of the PBPK model for our study[39]. Q is the plasma or blood flow,

CL is the clearance rate and U is the urinary excretion rate constant. The subscripts Lu, B, T, H, Li, Sp, RB, K indicates blood, lung, tumor, heart, liver, the rest of body, and kidney, respectively.

6.4 Two-pore Model

The two-pore model describes the flux of mAb from a capillary to the interstitium through diffusion and convection. The capillaries consist of large (~50 nm) and small (~10 nm) types of pores. The fluid recirculation rate J_{iso} isolates the large molecules such as mAb in the interstitial space[36]. The fluid and large molecules are diffused through the large pores while the fluid and small molecules are passed through the small pores. The fractional contribution of diffusion and convection to total large solute flux in the two-pore model was found by Rippe and Haraldsson[37].

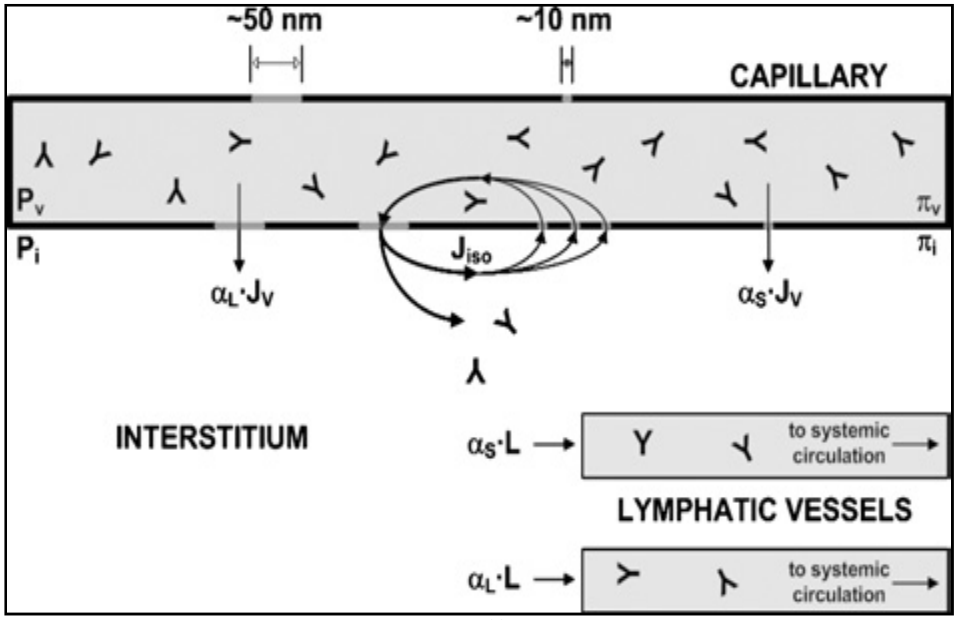

Figure 13: Two-pore model of mAb extravasation[36]. J_v is the fluid flux rate and L is the lymph rate in the interstitium. α_L and α_S are the fraction of the bulk fluid of the large and small pores ($\alpha_L + \alpha_S = 1$).

The transport of mAb across from the capillaries in each organ in the flux term J_{org} is defined by

$$J_{org} = J_{L,org}(1-\sigma_L)C_{v,org} + PS_{L,org}\left(C_{v,org} - \frac{C_{i,org}}{R_{org}}\right)\frac{Pe_L}{e^{Pe_L}-1} + J_{s,org}(1-\sigma_s)C_{v,org} + PS_{s,org}\left(C_{v,org} - \frac{C_{i,org}}{R_{org}}\right)\frac{Pe_s}{e^{Pe_s}-1} \quad \textbf{Equation 8}$$

$$J_{L,org} = J_{iso,org} + \alpha_L L_{org} \quad \textbf{Equation 9}$$

$$J_{S,org} = -J_{iso,org} + \alpha_S L_{org} \quad \textbf{Equation 10}$$

where PS is the permeability-surface area product PS (ml/h), J_L and J_S are the convection fluid flow rates of large and small pores respectively (ml/h), Pe is the Peclet number, $C_{v,org}$ and $C_{i,org}$ are the mAb concentration in the vascular and interstitial space respectively (M), R is the equilibrium distribution ratio (partition coefficient) of the mAb between the tissue and plasma, σ is the osmotic reflection coefficient which is the measure of the fraction of mAb molecules that does not pass through the pores of the blood capillary wall. The osmotic reflection coefficient is determined by the difference in hydrostatic and osmotic pressures[38].

6.5 Subcompartment Model

The intracellular subcompartment between vascular space and the interstitial space has the FcRn receptor. The FcRn receptor has a function of catabolism and elimination of mAb as well as protecting and recycling of mAb from degradation[38]. Figure 14 illustrates the protection and degradation of the mAb through Fc-Rn receptors. The degradation and the recycling of mAb are determined by the concentration of mAb[38]. As the binding sites are limited, an increasing concentration of mAb shortens the half-life of mAb in the body.

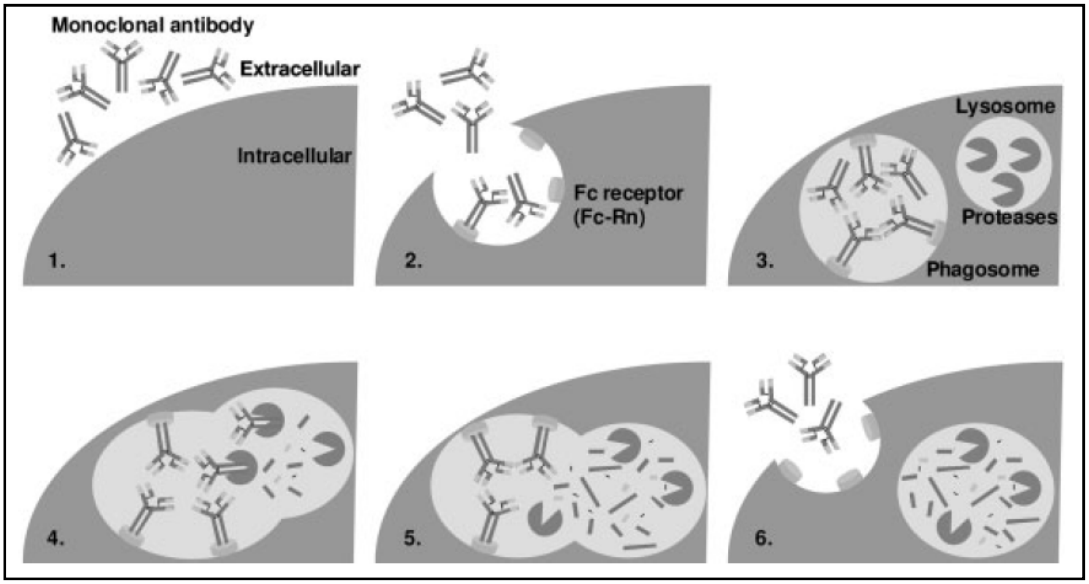

Figure 14: Schematic of antibody degradation by proteases and the protection of antibody by Fc-Rn phagosome. (1) Transporation of mAb to the extracellular space; (2) mAb are bound to Fc-Rn; (3) The lysosome containing protease binds with phagosome for degradation; (4) The protease attack the unbounded mAb; (5) The degraded products reside in the lysosome part; (6) The protected mAb by Fc-Rn are transported back to the cell membrane.

Fc-Rn-bound mAb are protected from intracellular degradation by the proteases, and they are recycled into the membrane. The unbound intracellular mAb are catabolized by the degradation rate k_{cat} in Figure 14. The degraded products are cleared from the organ compartment at the clearance rate of CL_{org}.

Figure 15 describes the interaction between the FcRn receptor and mAb in the endosome. The mAb is internalized by the internalized rate by the cell k_{int} in the endosome. The bound mAb onto the FcRn are recycled to the circulatory system as the rate of k_{rec}. The unbound mAb in the endosome are degraded by the rate of catabolism k_{cat}. The catabolites C_m, as the result of the catabolism from the endosome, are cleared by the rate of CL_{org} and are returned to the circulation of the body. Eventually all the catabolites will be excreted by the kidney.

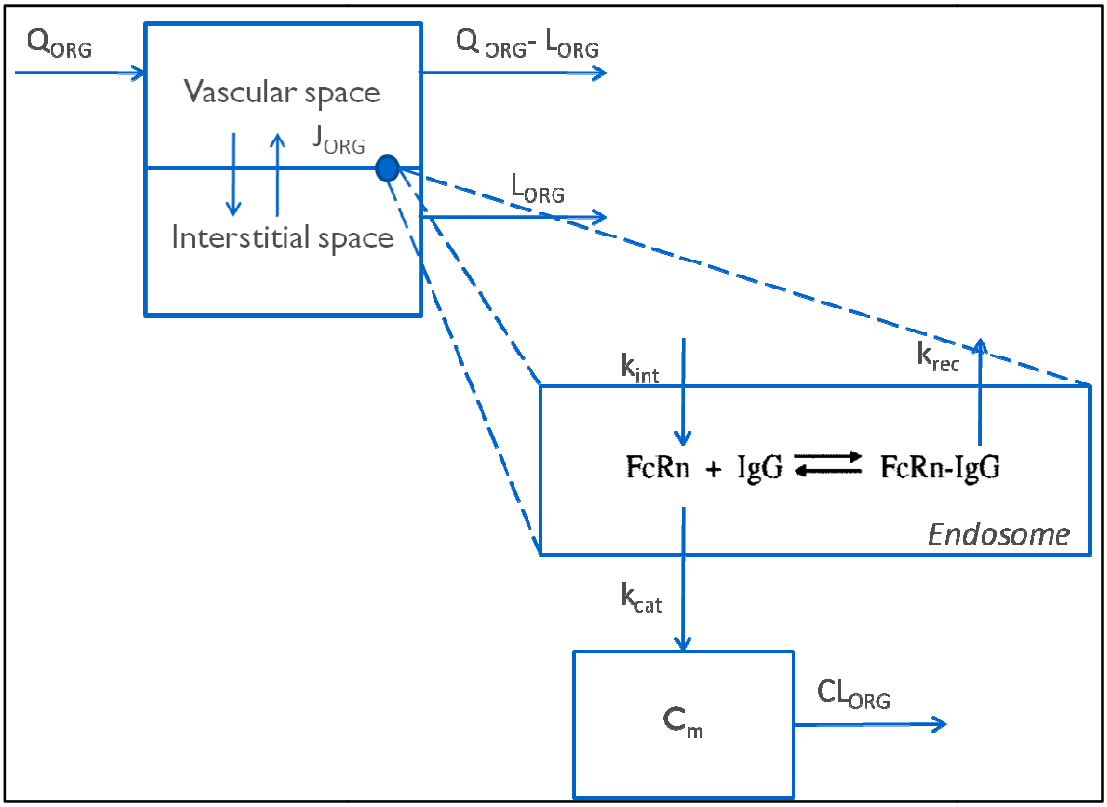

Figure 15: The schematic diagram of the subcompartment model

6.6 Determining the Initial Dose

One interesting part of the model obtained from the set of differential equations is the amount of the bounded antibodies in the tumor cells, $q_{3,6}$. Tumor content (TC) is defined as the amount of the antibodies in the tumor-bound compartment at a given time[23]. The maximum tumor content (max TC) can be obtained by

$$Maximum\ Tumor\ Content\ (\%) = \frac{q_{3,6}}{D} \times 100 \qquad \textbf{Equation 11}$$

where D is the initial dose in moles. The max TC is used to determine the efficient amount of the initial dose. As the dosing amount was increased, the tumor receptor approached the saturation point where no more free antibodies can be bound.

6.7 Treatment Varied with the Tumor Volume

The effect of tumor size on cancer treatment needs to be considered. The sizes of the tumor were selected as 0.01, 0.015, 0.02, and 0.025 L at an initial dose of 6×10^{-9} moles. The parameters and values used in this model are shown on Appendix A.

The distribution of the antibodies through the body can be studied to determine NIR emission time to SWNTs while considering the size of tumors.

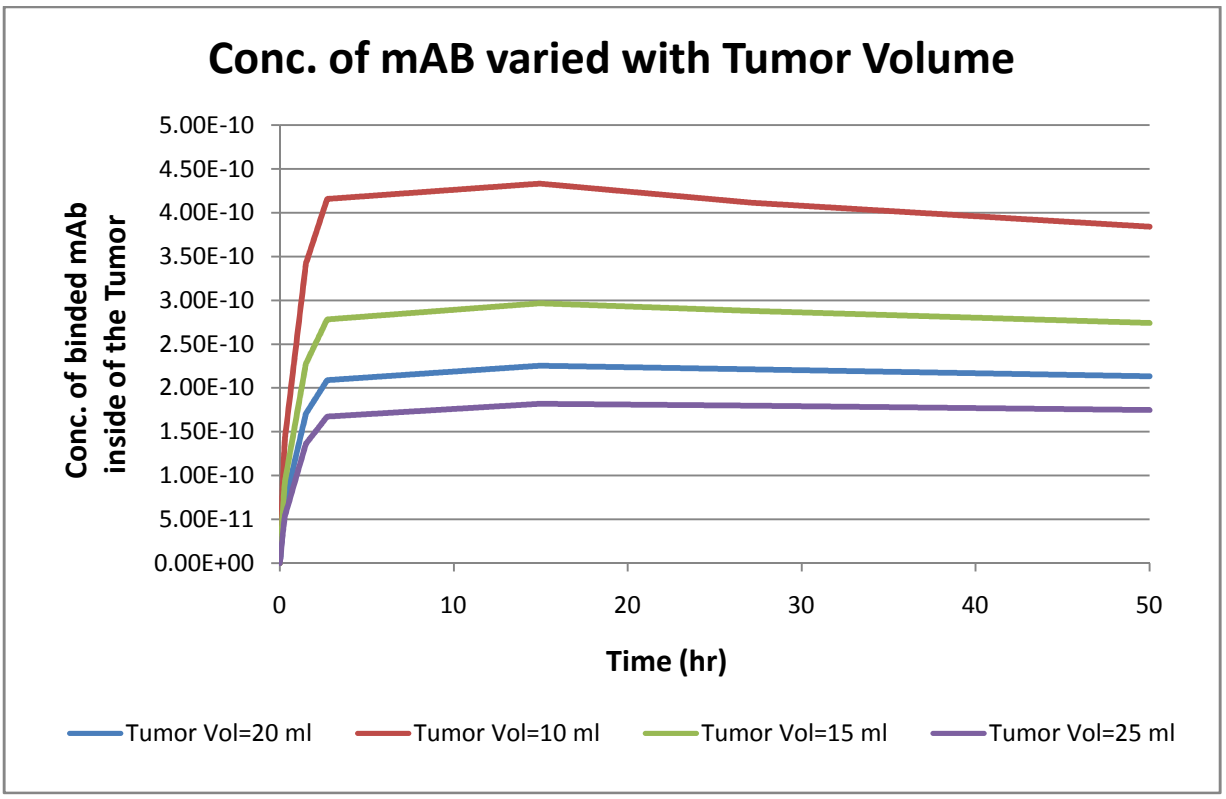

Figure 16: The effect of the amount of bounded antibodies on the size of the tumor

Figure 16 shows that the amount of the bounded antibodies was decreased as the size of the tumor volumes are increased. The relationship between tumor size and number of antibody receptors on its surface is directly proportional. The concentration of specific binding sites on tumor is an independent variable (k_{fag}) of the volume of the tumor size and the interstitium and vascular space of the tumor also increased which results in having less capacity to uptake the antibodies. The time required to reach the maximum TC is about 15 hours after injection of the initial dose. Therefore, the NIR radiation treatment can be began after 15 hours to maximize the benefit.

The percentages of the tumor content also were determined in Figure 17. Over 3 % of the initial dose of 6×10^{-9} moles were internalized into the tumor cells when the tumor volume was 0.025 L. The tumor contents values are used to calculate the initial amount of SWNTs.

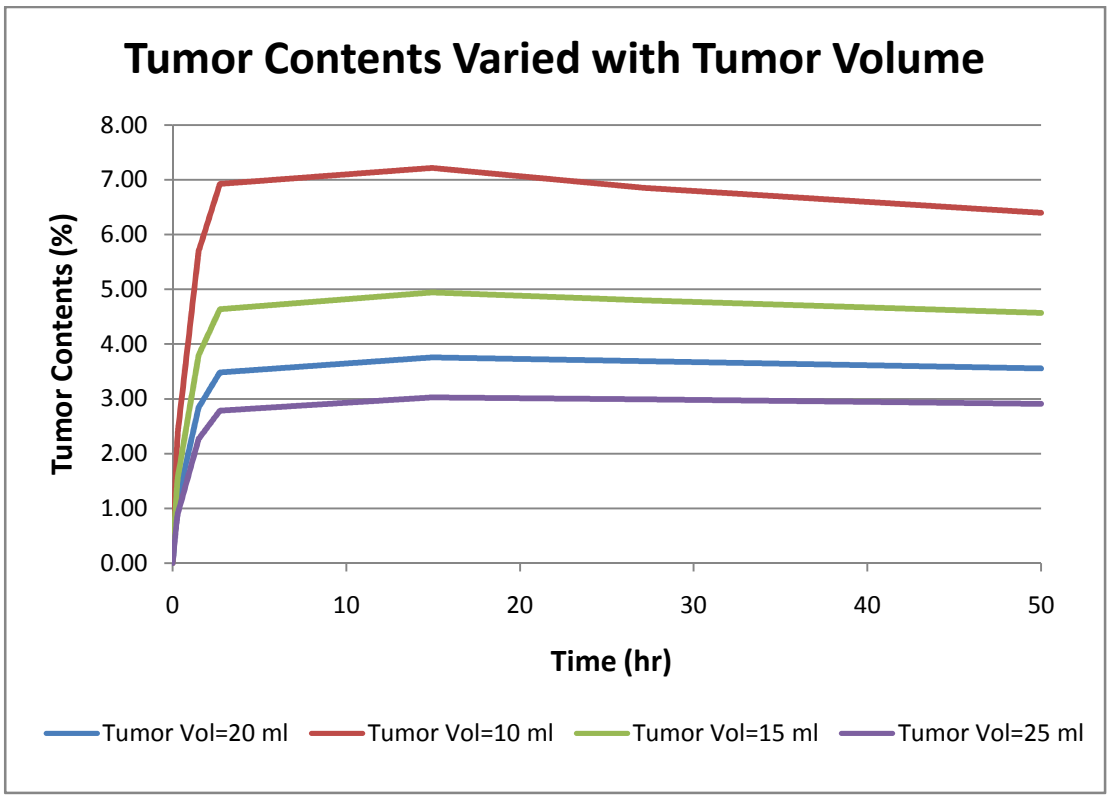

Figure 17: The effect of the TC% on the size of the tumors

6.8 Models for Photothermal Therapy

Since the amount of the initial dose and the emitting time of the NIR are determined by the antibiotic treatment, the optimal quantity of the SWNTs can be defined. After the monoclonal antibodies conjugated with the SWNTs are attached onto the receptors on the tumors, the SWNTs are internalized through the cytokine receptor[24]. Kam, N. et al. found the range of the wavelength of near-infrared to destroy the SWNTs between 700 and 900 nm. The energy range of 0.8~3.5 W/cm^2 for three minutes was used to heat the SWNTs[25].

In this literature, the absorbance of SWNTs at the wavelength of 808 nm found to be maximized; therefore 808 nm was used to increase the temperature of the SWNTs. The temperature range of the heated target tumors are increased up to 55~90°C. The energy used in the destruction of one cancer cells is about 200 nW per cell. The thermal gradient in the SWNTs is extremely steep (~10^6-10^9 C m^{-1}), resulting in a very rapid and localized heating high

temperatures. The steep thermal gradients localize the heating effect of the SWNTs so that the effects would not harm the adjacent normal cells while the tumor cells are destroyed[8].

The following assumptions were made in order to determine the quantity of the SWNTs:

1) 100 % of the energy emitted by the NIR laser would be absorbed into the SWNTs.
2) The length and diameter of one SWNT are the same as Kam, et al. used in the literature[25]. The length and diameter of one SWNT are 150 nm and 1.2 nm, respectively.
3) The energy requirement to kill one cancer cell is equally applied to all the cancer cells, which is 200 nW per cell.
4) The shape of tumor is a sphere.
5) The biggest diameter of one cancer cell in the tumor is 200 µm. This assumption is based on the furthest distance that the tumor cell can move from the blood vessels. The cells farthest from the blood vessel would suffer from the lack of the supply of oxygen and nutrients. This phenomenon is called hypoxia[26].

6.8.1 Calculating the Number of Cancer Cells in a Colony of Tumor

The major parameter used for the photothermal therapy is the energy requirement to kill one cancer cell, which is 200 nW/cell. The number of cancer cells in a colony is required to calculate the number of the SWNTs required in order to destroy the tumor. However, exact number of cancer cells in a colony of tumor cells is very difficult due to the heterogeneous characteristic of tumors. Based on the assumption 5), the biggest diameter of one cancer cell was chosen as 200 µm. Since the shape of the volume is a sphere, the diameter of the tumors can be calculated by

$$\mathbf{N_{min}} = \frac{\mathbf{V_{tumor}}}{\frac{\pi}{6}\times \mathbf{D_{cell}^3}} \qquad \textbf{Equation 82}$$

where N_{min} is the number of the cancer cells in a tumor colony, V_{tumor} is the volume of the tumor, and D_{cell} is the diameter of one cancer cell. Since the D_{cell} is determined to 200µm, N_{min} is the minimum number of cells in a tumor colony.

6.8.2 Calculating the Number of Cancer Cells Using the Random Number Method

Although the minimum number of cancer cells are found using Equation 13, a more accurate number of cancer cells needs to be determined. F. L. Meyskens, Jr., et al. developed the equation for the number of cells in a tumor colony followed by[27]

$$\ln(\mathbf{N_{cells}}) = \mathbf{0.874} - \mathbf{2.804} \cdot \mathbf{D_{cell}} + \mathbf{2.378} \cdot \ln(\mathbf{D_{tumor}}) \qquad \textbf{Equation 93}$$

where D_{tumor} is the diameter of the tumor. D_{tumor} can be calculated by

$$\boldsymbol{D_{tumor}} = \sqrt[3]{\boldsymbol{V_{tumor}} \cdot \frac{\mathbf{6}}{\boldsymbol{\pi}}} \qquad \textbf{Equation 104}$$

where V_{tumor} is the volume of tumor. The same tumor volumes were selected from the antibiotic treatment varied with the tumor volume; 0.01, 0.015, 0.02, and 0.025 L. The N_{cells} value is varied with D_{cell} and D_{tumor} based on the Equation 11. D_{cell} is not known; therefore the random number method should be used to calculate N_{cell}. It was assumed that the range of the distribution of diameter of cancer cells inside of the tumor colony is between 50 and 200 µm. The histogram below shows the result after generating random numbers.

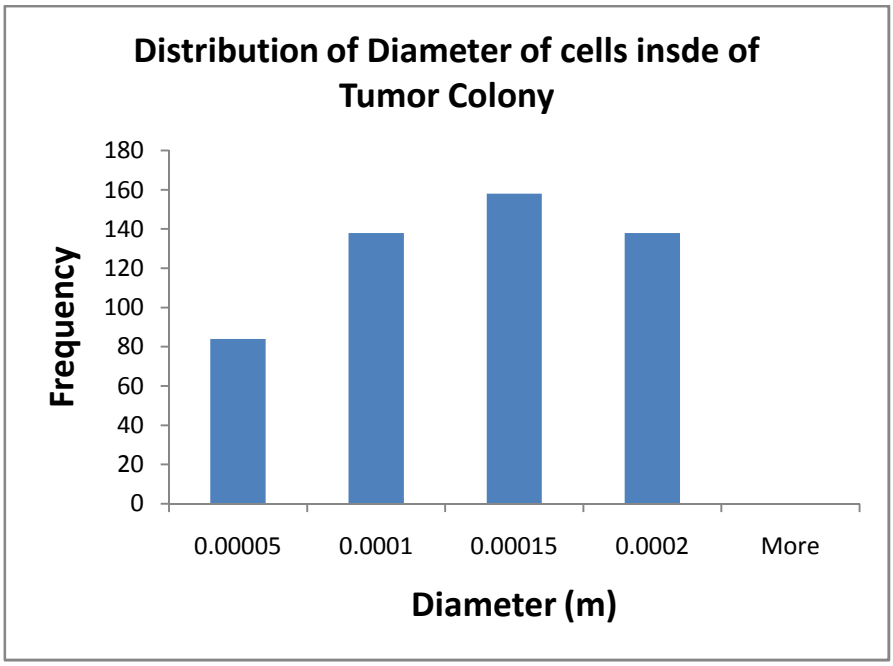

Figure 18: The histogram of random number generation for the diameter of one cancer cells

N_{cells} now can be calculated using Equation 13 and D_{cell} which was randomly generated. The histogram was generated again to choose the highest frequencies of N_{cells}. A more detailed explanation is covered in Appendix D.

6.8.3 Calculating the Energy Used in the Destruction of the Tumor Cells

The energy used in the destruction of the tumor cells were calculated by

$$\boldsymbol{E_d = 0.8 \cdot N_{cells}} \qquad \textbf{Equation 115}$$

where E_d is the destruction of the tumor cells in the unit of W, the value of 0.8 W·cm^{-2} is the energy absorbed into the SWNTs, and N_{cells} is the number of the cancer cells in tumor colony.

The number of the SWNTs (N_{SWNT}) required destroying the tumor cells can be calculated followed by

$$\boldsymbol{N_{SWCT} = \frac{E_d}{E_{emit}}} \qquad \textbf{Equation 126}$$

where the energy emitted by one SWNT, E_{emit} can be calculated by

$$\boldsymbol{E_{emit} = 0.8 \times \pi \times L_{SWCNT} \times D_{SWCNT} = 0.8 \times A_{SWCNT}} \qquad \textbf{Equation 137}$$

where L_{SWNT} is the length of one SWNT, D_{SWNT} is the diameter of one SWNT, and A_{SWNT} is the surface area of one SWNT.

The number of the SWNTs, N_{SWNT} can be expressed as the mole number followed by

$$\boldsymbol{N_{SWCNT,mole} = N_{SWCNT}/N_{Av}} \qquad \textbf{Equation 148}$$

where N_{Av} is the Avogadro's number, which is 6.23 ×10^{23}.

Finally, the initial dose of SWCNTs, D_{SWNTs} can be determined by

$$\boldsymbol{D_{SWCNTs} = N_{SWNT,mole}/(\frac{TC}{100})} \qquad \textbf{Equation 19}$$

where TC is the percentage of tumor content of the antibodies. The value of TC indicates the percentage of antibodies that reach the tumors. The same ratio of TC percentage is shared since the SWNTs and the antibodies are conjugated.

All the values that were calculated are summarized in Table 3.

	Number of cells in a colonies			
Tumor Vol. (L)	0.01	0.015	0.02	0.025
Diameter (m)	2.67×10^{-2}	3.06×10^{-2}	3.37×10^{-2}	3.63×10^{-2}
(minimum)	2,387,324	3,580,986	4,774,648	5,968,310
(random)	1,091,776,197	1,505,619,715	1,891,254,894	2,257,186,280
	Energy used in the destruction of tumor cells (W)			
(minimum)	0	1	1	1
(random)	218	301	378	451
	Number of SWCNT required to destroy the tumor cells			
(minimum)	1.06E+11	1.58E+11	2.11E+11	2.64E+11
(random)	4.83E+13	6.66E+13	8.36E+13	9.98E+13
	Total amount of SWCNT (mol)			
(minimum)	1.75E-13	2.63E-13	3.50E-13	4.38E-13
(random)	8.01E-11	1.11E-10	1.39E-10	1.66E-10
	TC value of Antibodies (%)			
	7.21	4.94	3.75	3.02
	Initial dose SWCNT required (mole)			
(minimum)	2.43E-12	5.32E-12	9.34E-12	1.45E-11
(random)	1.11E-09	2.24E-09	3.70E-09	5.48E-09
	Initial dose antibody used (mole)			
	1.11E-09	2.50E-09	4.00E-09	6.00E-09

Table 3: Summary of values for photothermal therapy requirements

All those values are calculated based on the N_{min} (minimum) and N_{cells} (random). N_{cells} was determined by generating the random numbers.

6.8.4 Calculating the mAb Concentration in the Body

The results of the PBPK model show the concentration of the monoclonal antibodies in the body. Parameters for the physiochemical properties of the tumors, normal cells, and other tissues were taken from various literatures.

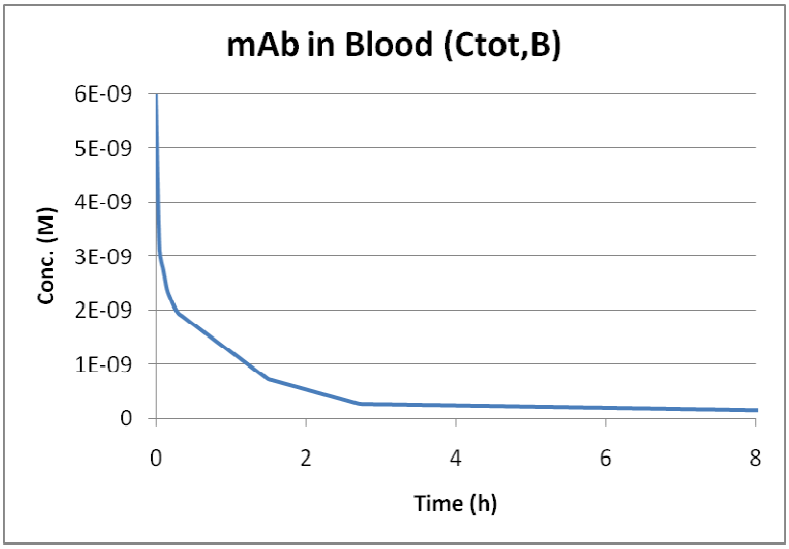

Figure 19: Concentration of mAb in the blood

In Figure 19, the concentration of the mAb starts out very high in the blood upon injection. As the mAbs travel out of the leaky vasculature and bind to the tumors, the concentration in the blood decreases. Catabolism of the mAb will eventually occur, thereby further decreasing the concentration to approach zero.

Figure 20 illustrates the mAb concentration in the tumor. Its concentration in the tumor rises sharply due to its targeting nature. After a period of time, catabolism of the mAb will account for the slow decrease in concentration.

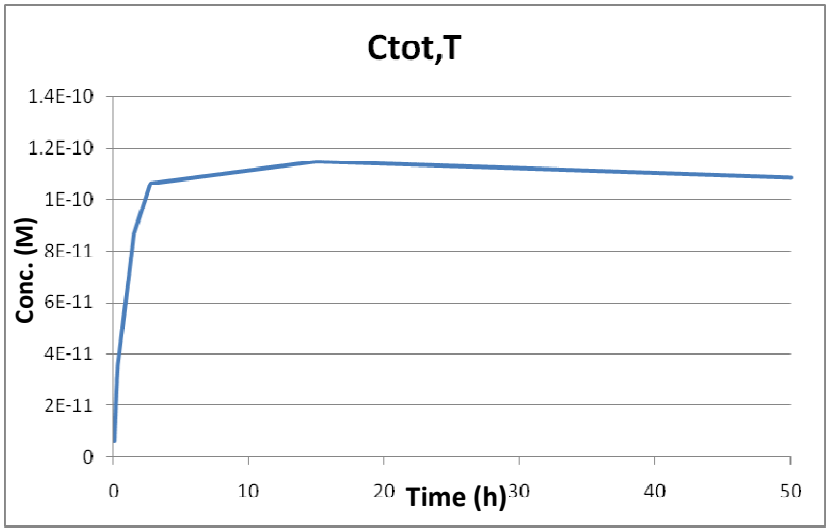

Figure 20: Concentration of mAb in the tumor

The concentration of unbound or free mAb in the interstitium is represented below in Figure P. It follows a similar trend as in Figure 21. The decreasing concentration of free mAb in the interstitium can be attributed to binding to the tumor or catabolism.

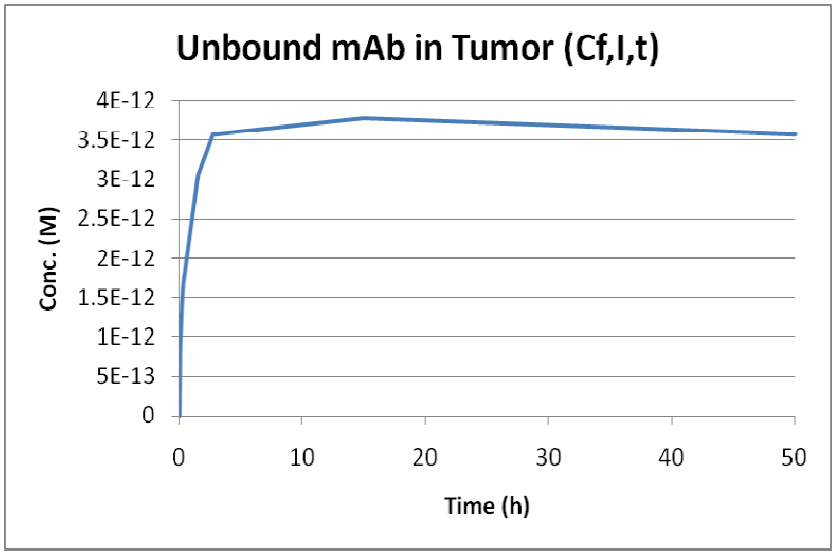

Figure 21: Concentration of unbound mAb in the tumor

Figure 22 shows the concentration of bound mAb in interstitium.

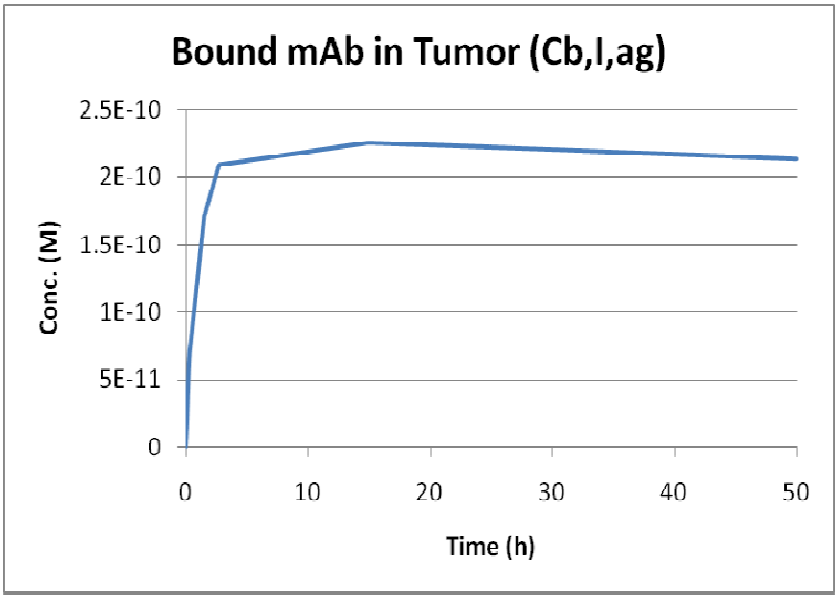

Figure 22: Concentration of bound mAb in the tumor

In Figure 23, the ratio of the initial concentrations of the mAb to the total concentration is plotted for the blood, tumor, and other organs in the body. The concentration in the rest of the body appears to plateau. This may not be the most accurate model since the literature combined the "rest of the body" into a separate entity. In order to gain a more accurate model, each part would need to be considered separately so that the appropriate parameters can be included in the model.

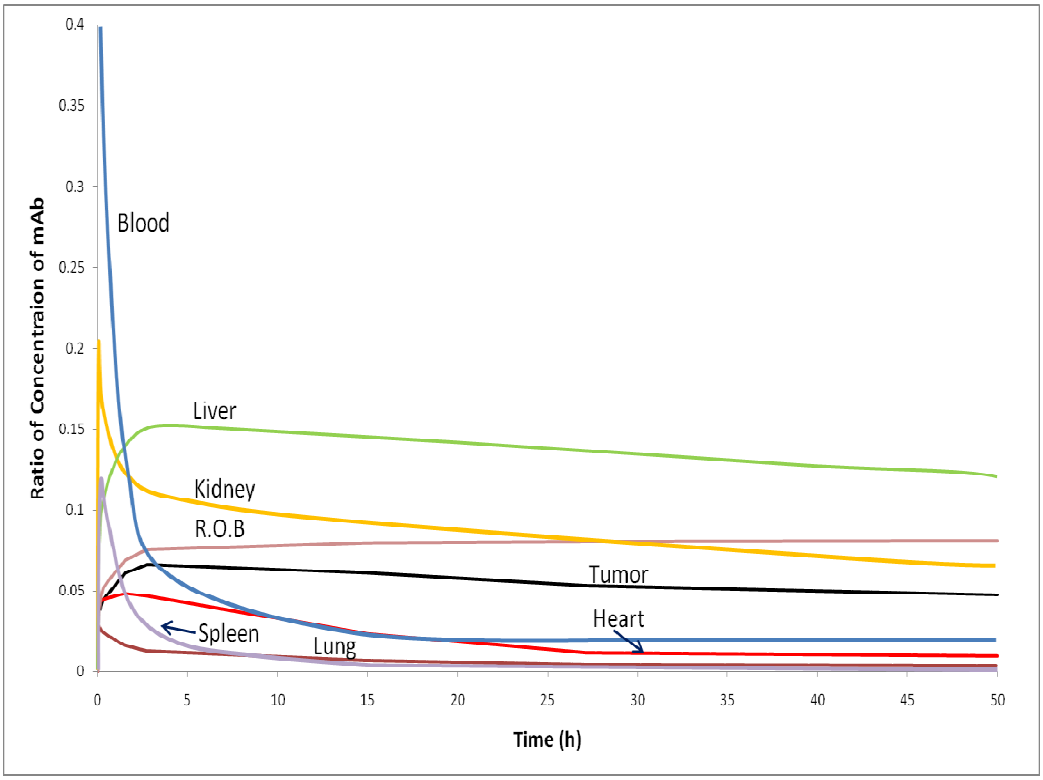

Figure 23: Ratio of concentrations of mAb in selected organs of the body

It is also important to know the concentration of drug in surrounding normal cells before the NIR radiation. There is a risk of heating up the normal adjacent cells if the concentration of mAb-SWNT conjugate is relatively high around the tumor. The concentration of the drugs in the adjacent cells of tumor was calculated beginning with an assumption that the concentration of the adjacent cells is the ratio of the volume of the adjacent cells of the tumor to the volume of the rest of body (ROB). The concentration in the ROB was calculated by the MathCad software. Additional assumptions were made in order to calculate the concentration of the adjacent cells.

The volume of the adjacent cells was “wrapped around” the tumor in the thickness of 5 cm as shown in Figure 24.

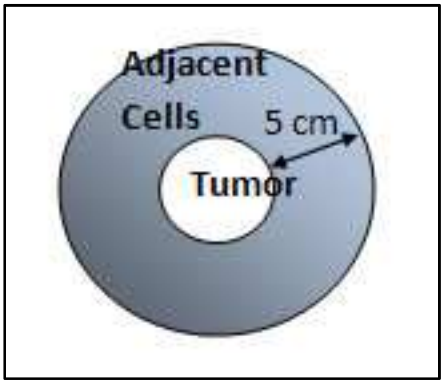

Figure 24: A schematic diagram of the volume of the adjacent cells. The thickness of the adjacent cells surrounded by the tumor is defined to be 5 cm.

The volume of the adjacent cells can be calculated by

$$V_{Adj} = \frac{4}{3}\pi\left((R_{tumor} + 5) - R_{tumor}\right)^3 \qquad \textbf{Equation 20}$$

As mentioned above, the concentration of the drug in the adjacent cells is the ratio of the volume of the adjacent cells to the ROB. The concentration in the adjacent cells can be calculated by

$$C_{adj} = C_{ROB}\frac{V_{Adj}}{V_{ROB}} \qquad \textbf{Equation 21}$$

where C_{ROB} is the concentration of ROB which was found by the MathCad software, and V_{ROB} is the volume of ROB, which is 61.2 L from the literature value[39].

The plot of the concentration of the drug in the tumor and adjacent cells as the function of time is shown below.

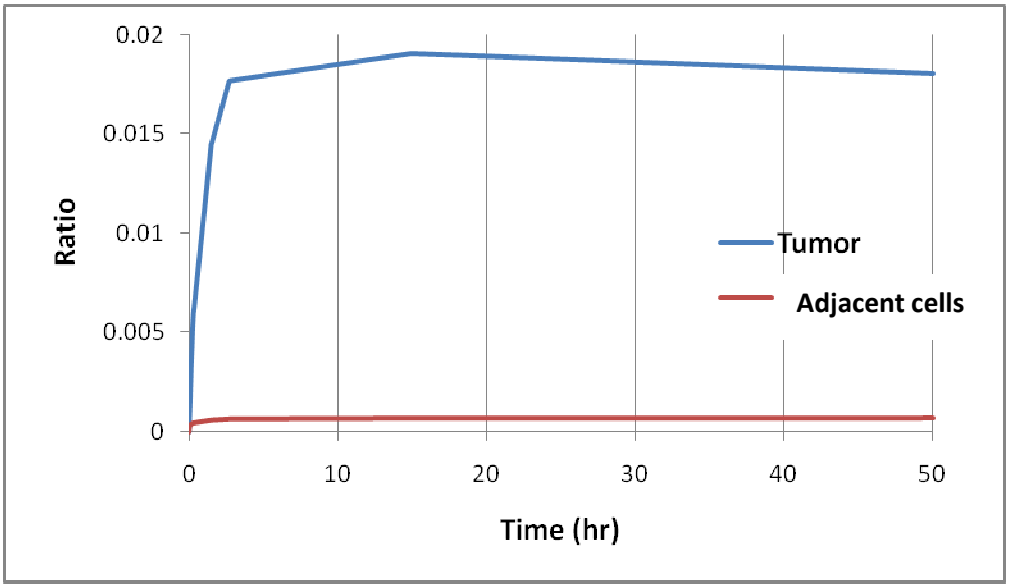

Figure 25: Concentration of mAb-SWNT in the tumor and adjacent normal tissues

The concentration of drug in the adjacent cells is significantly small compared to in the tumor cells even though the sizes of the adjacent cells are much bigger than the tumor. As the mAb pass by the surrounding tissue, they become uptaken by the tumor. In the model, it is assumed that the mAb would not bind the adjacent cells. As explained in Section 6.1, this would not be the physical case since normal cells have been shown to express the HER2 receptor. The probability of uptake by normal cells was calculated to be very small.

6.8.5 Finite Difference Method

It is desired to know the death ratio of cancer cells in the tumor as the NIR radiation treatment is proceeding. The death of cancer cells is reached by increasing the temperature of cancer cells to the critical temperature. If the spherical shape of tumor is assumed to be a lump system, meaning that the temperature inside of the tumor is same as the surface temperature, the death rate would be 100% after the temperature of the 'lump' tumor achieves the critical temperature.

Transient heat transfer in the radial direction only is able to simulate the temperature gradient inside of the tumor. There are two schemes to describe the transient heat transfer: explicit method and implicit method. The explicit method predicts the future temperature value in terms of the current temperature value for each time iteration. The implicit method predicts the future temperature value in terms of the current temperature value along with the future temperature value. The explicit method is chosen because the computational time is shorter than the implicit method. However, the use of the explicit method requires the consideration of the stability criterion. Therefore, the stability criterion was taken account in the simulation. The equations are further explained in later sections.

There are several assumptions for this simulation. The first one assumes a spherical tumor. The sphere was exposed to the convective environment, natural convection, by water which is the body temperature at 37° C. The sphere was divided into discrete spherical layers. Each discrete layer is assumed to be at uniform temperature, and each temperature represents the node in the one-dimensional system. There are three different types of nodes in the sphere: the central node, internal node, and outside surface node. The division of the nodes considers the different types of geometry. The central node is located in the core, and the geometry is sphere. The interior nodes and the surface node have hollow sphere geometry. The heat transfer of interior nodes is only governed by conduction whereas the outside surface is by conduction from the interior nodes and convection from the outside of medium.

An energy balance on each of the nodes yields the finite differences equation below. A full derivation of the equation is detailed in Appendix H.

$$T_m^{i+1} = \frac{4\pi k \Delta t}{\rho V c_p \Delta r}\left(r - \frac{\Delta r}{2}\right)^2 (T_{m-1}^i + T_m^i) + \frac{4\pi r^2 h \Delta t}{\rho V c_p}\left(T_m^i + T_\infty\right)^2 + \frac{g \Delta t}{\rho c_p} + T_m^i \qquad \textbf{Equation 22}$$

MATLAB 7.4 was used to simulate the finite difference equations. The thermophysical properties of the tumor were chosen from literature. The number of nodes was chosen as 100, and the thermophysical properties of water were chosen at 37°C. The time step was 0.01 sec. This time value was sufficiently small to give a convergent solution. The temperature contour

plots from the finite difference equations are shown below for 1 min, 2 min, and 3 min of heating.

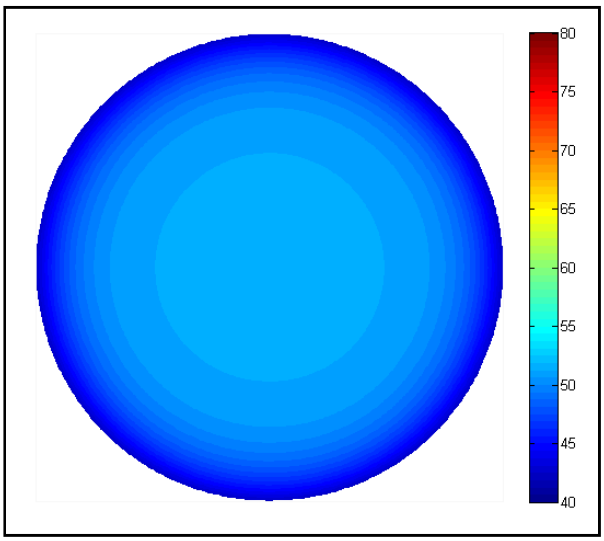

Figure 26: Temperature of the tumor after 1 minute of NIR irradiation

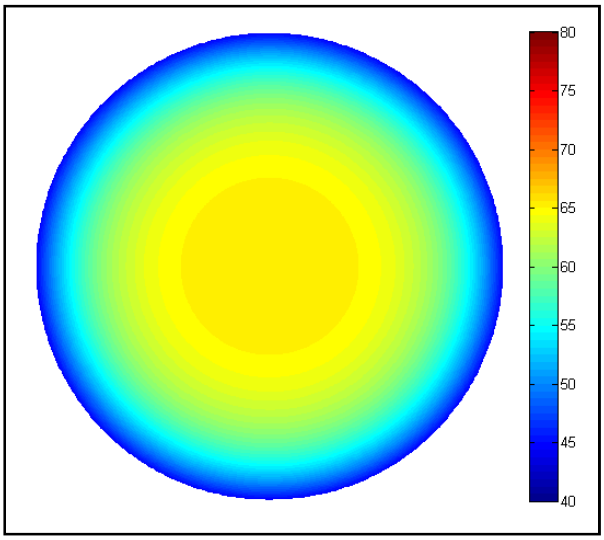

Figure 27: Temperature of the tumor after 2 minutes of NIR irradiation

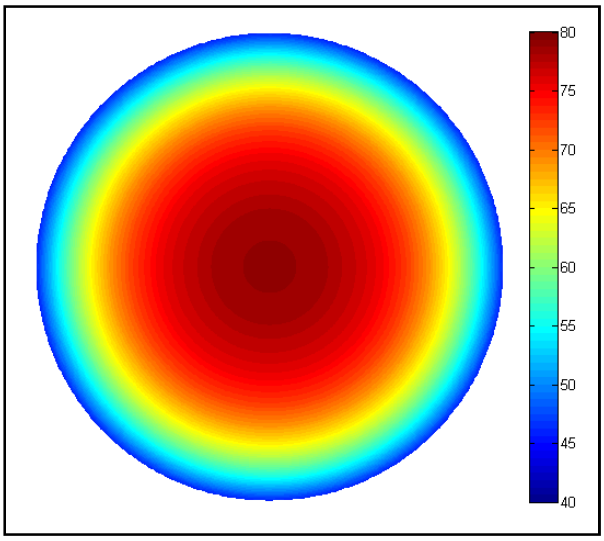

Figure 28: Temperature of the tumor after 3 minutes of NIR irradiation

After three minutes of NIR laser treatment, the center temperature was about to 85°C whereas the temperature of the surface of tumor was about 40°C. The death rate was determined using the temperature contour plots shown above. When the temperature of cancer cells exceeds 57°C, they are considered dead. The number of cells in each nodal layer was determined by multiplying the density of cancer cells in the entire tumor by the volume of each nodal layer. The nodal layer temperature surpassed the critical temperature; all of the cells within that nodal layer were killed. Therefore the total proportion of dead cancer cells can be calculated from the number of dead cells within nodal layers at temperatures greater than the critical temperature. The plot of the death rate can be shown below in Figure 29.

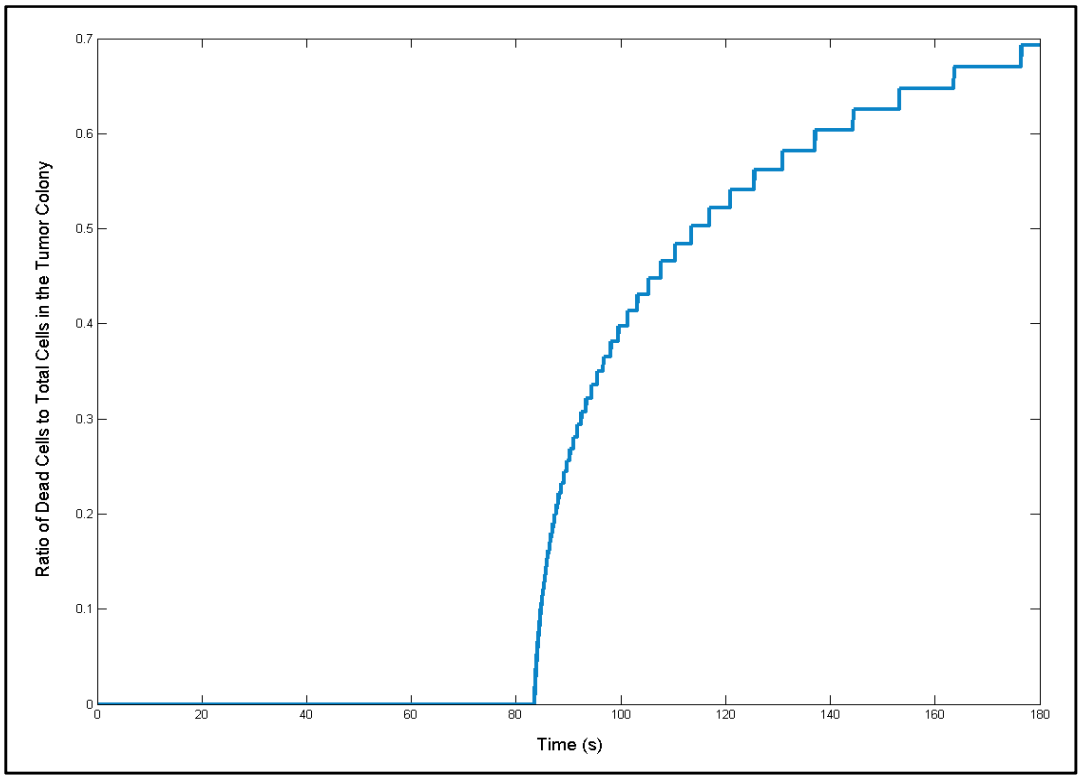

Figure 29: Proportion of dead cancer cells to total cells in a tumor colony as a function of time

The figure shows that approximately 70% of cancer cells in a tumor colony were dead after three minutes of NIR radiation. The cancer cells began to die after 80 seconds of NIR radiation. Three minutes was selected for this simulation based on literature[8]. For NIR radiation longer than three minutes, the risk of exceeding 100°C in the center temperature of the tumor increases. It is not desired to have above the bubbling point inside of the cells due to evaporation of the cell medium.

The cooling time requirement after NIR radiation

The time required for the tumor cells to return to the ambient temperature was also considered. It is assumed that the tumor volume was not reduced based on the ratio of dead cells to the total cells of tumor. The MATLAB code was modified by removing volumetric heat generation rate terms from the finite difference equations. The temperature contour plot at 1, 5, 10, and 15 minutes are shown below.

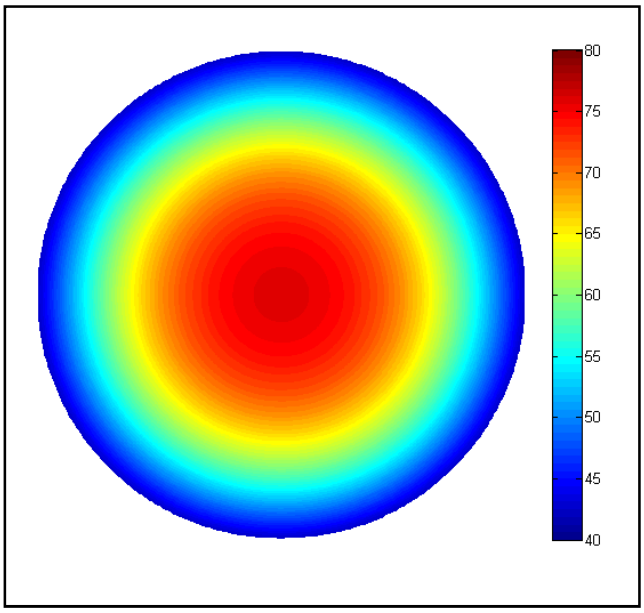

Figure 30: Temperature of the cooling tumor after 1 minute following NIR irradiation

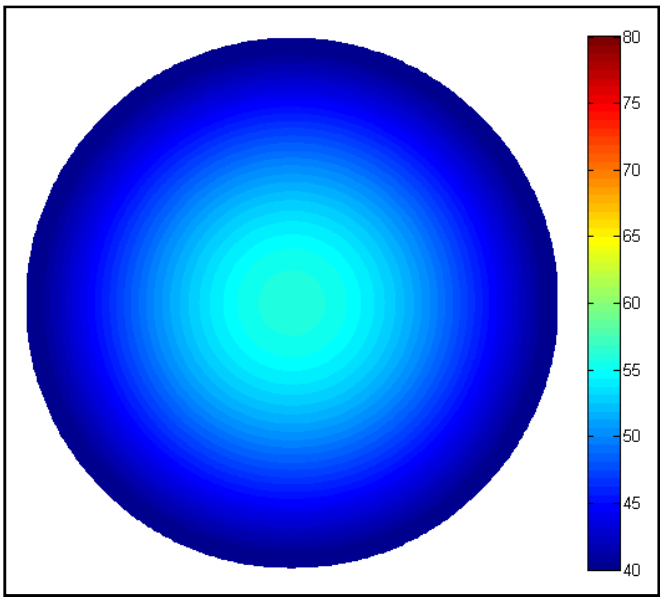

Figure 31: Temperature of the cooling tumor after 5 minutes following NIR irradiation

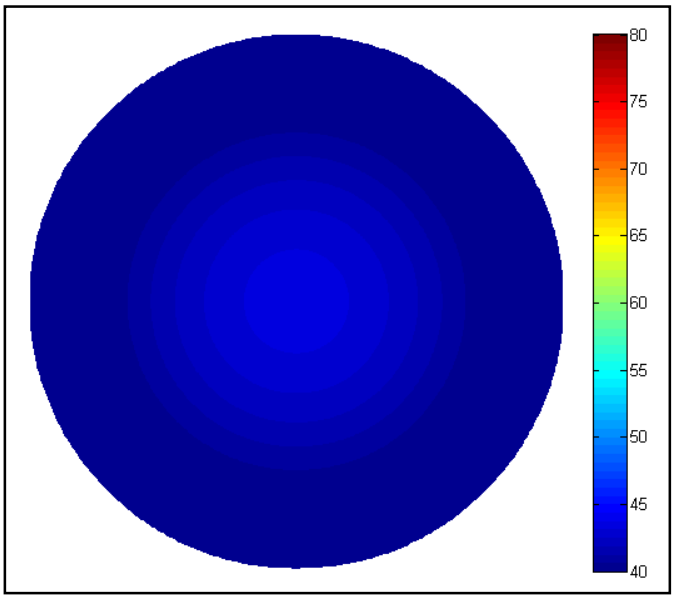

Figure 32: Temperature of the cooling tumor after 10 minutes following NIR irradiation

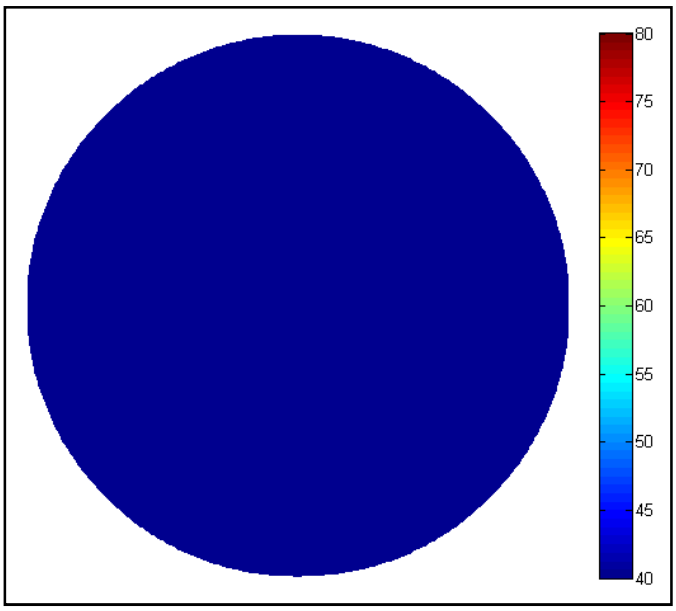

Figure 33: Temperature of the cooling tumor after 15 minutes following NIR irradiation

After fifteen minutes, most of the cancer cells reached ambient temperature. Therefore fifteen minutes is the time at which a second NIR radiation treatment may be done.

The radiation and cooling cycle shown in the plot enables for the determination of the appropriate radiation treatment time and cooling time based on transient heat transfer and

death rate model. Each cycle shown in Figure 34 below estimates the death ratio of 70% of the cells.

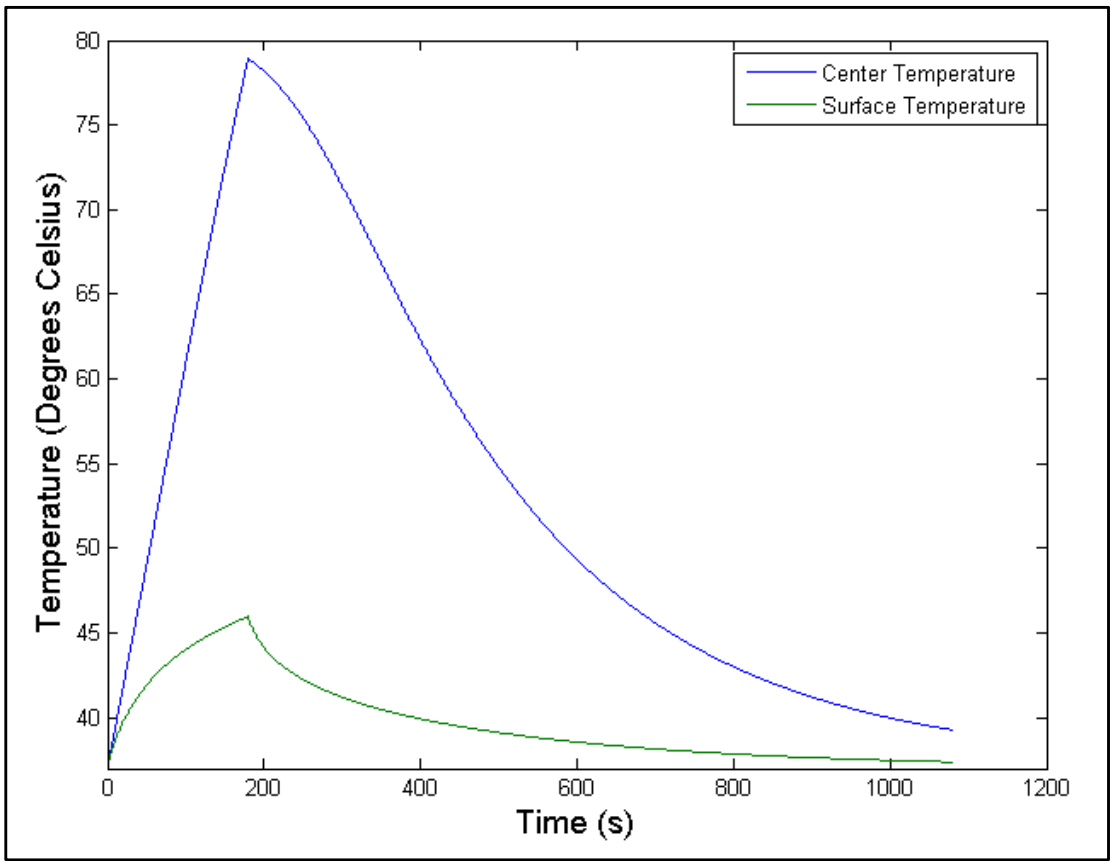

Figure 34: Temperature profile of cancer cells during and after NIR irradiation

Figure 34 shows that 18 total minutes is required for the cancer cells to reach near the ambient temperature. After 18 minutes, it is safe to begin the second NIR radiation because the core temperature inside of the tumor is close to the ambient temperature.

The cooling plot with consideration of tumor volume reduction

If the tumor volume size is reduced by the maximum death ratio after the NIR treatment, the cooling time to reach the ambient temperature will be significantly reduced. The temperature contour plots at 1, 5, and 10 minutes are shown in the figures below.

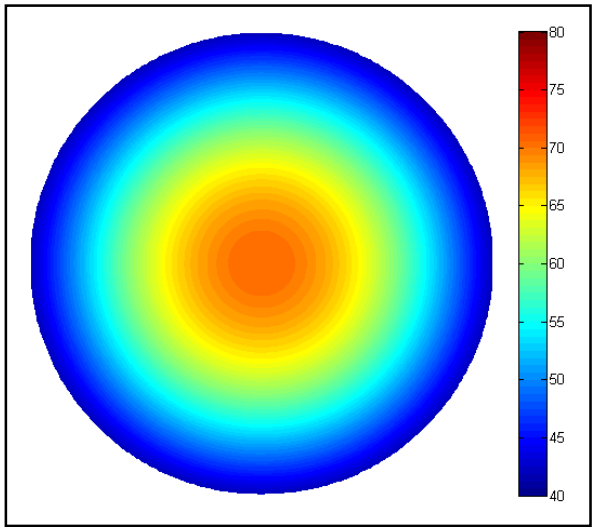

Figure 35: Temperature contour plots of a cooling tumor with consideration of volume reduction after 1 minute following NIR irradiation

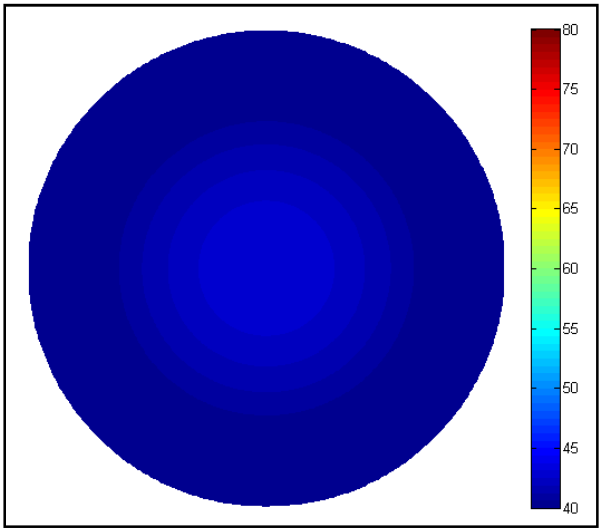

Figure 36: Temperature contour plots of a cooling tumor with consideration of volume reduction after 5 minutes following NIR irradiation

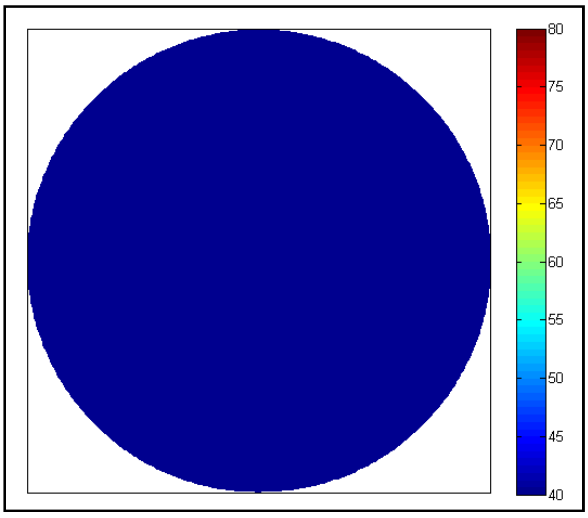

Figure 37: Temperature contour plots of a cooling tumor with consideration of volume reduction after 10 minutes following NIR irradiation

The contour plot with reduced tumor volume shows ten minutes was enough time for the tumor to reach to the ambient temperature.

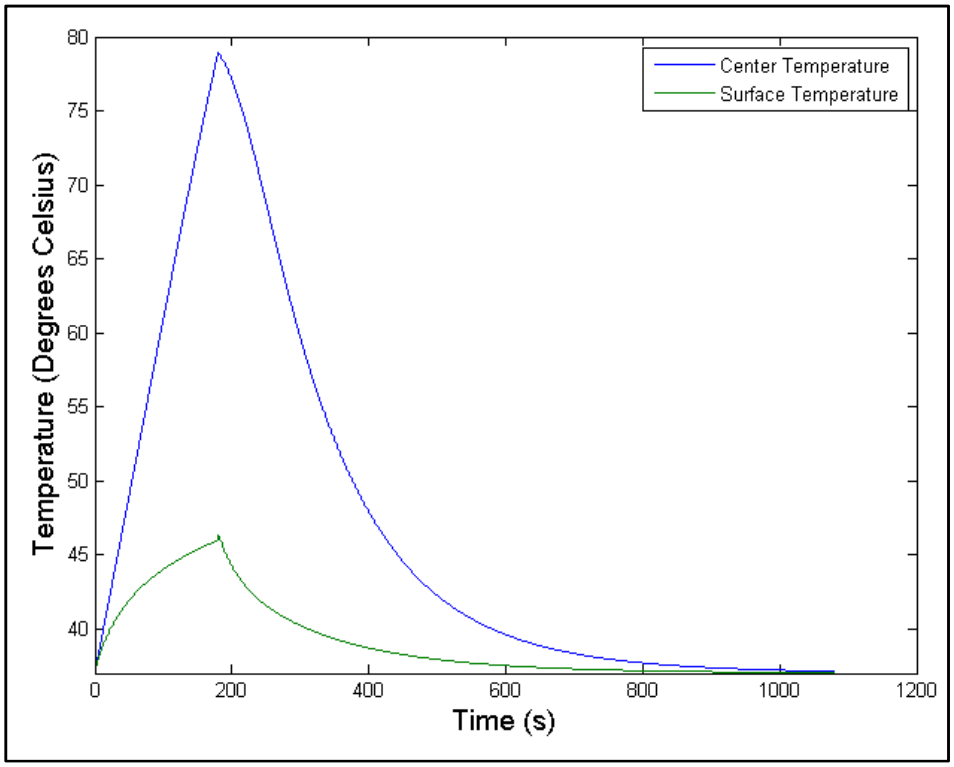

Figure 38: Temperature profile of cancer cells during and after NIR irradiation (assuming tumor volume reduction)

Under the assumption of tumor volume reduction following NIR laser treatment, Figure 39 shows that 18 minutes after irradiation is required for the cancer cells to reach near the ambient temperature. After about 13 minutes, the core temperature was sufficiently low, therefore, the second NIR treatment can commence to kill more cancer cells.

7. Production of Monoclonal Antibodies and Single-walled Carbon Nanotubes

In order to successfully market the treatment, its large-scale production must be considered. Due to its complexity within the time constraints of this project, the SWNTs will be purchased from Southwest Nanotechnologies and will be regarded as raw material. The large-scale production of monoclonal antibodies and its conjugation with SWNTs are discussed below. The scale-up values were based on literature and were used to figure equipment costs, which were then used in the economic analysis discussion in Section 8.3.

7.1 Large-scale Production of Monoclonal Antibodies

One method of the production of therapeutic monoclonal antibodies comprises of three sections: a bioreaction section, a recovery section, and a purification section[13].

A serum-free and low protein content media powder is mixed with water in a stainless steel tank and is then sterilized by a polishing filter. Cells expressing the therapeutic monoclonal antibody are cultivated for a week in a stirred tank bioreactor operating in fed-batch mode[13].

The biomass and other contents are passed through a membrane diafilter. A molecular weight cutoff ultrafilter concentrates the solution, which is then passed to the purification section[13].

The purification section uses a series of chromatography columns to remove contaminants and to purify the solution. An affinity chromatography column is used to remove most of the impurities in the mixture. Then the mixture is passed through a cation exchange column, where

a linear gradient elution removes charged particles to concentrate the solution. The next step is the hydrophobic interaction chromatography step. This operation further purifies the solution and prepares it for the addition of glyercol, which is used for product stability. A flowsheet of a typical large-scale monoclonal antibody production is shown in Figure 39[13].

The numbers for the large-scale production were based on the projected population (see Section 8.2), the concentration dosage of monoclonal antibodies suggested from the mathematical model, and the estimated number of annual treatments per patient. They were then compared to the textbook values, and a ratio was used to scale up to the desired large-scale production rate, which is 2 g of monoclonal antibodies per day.

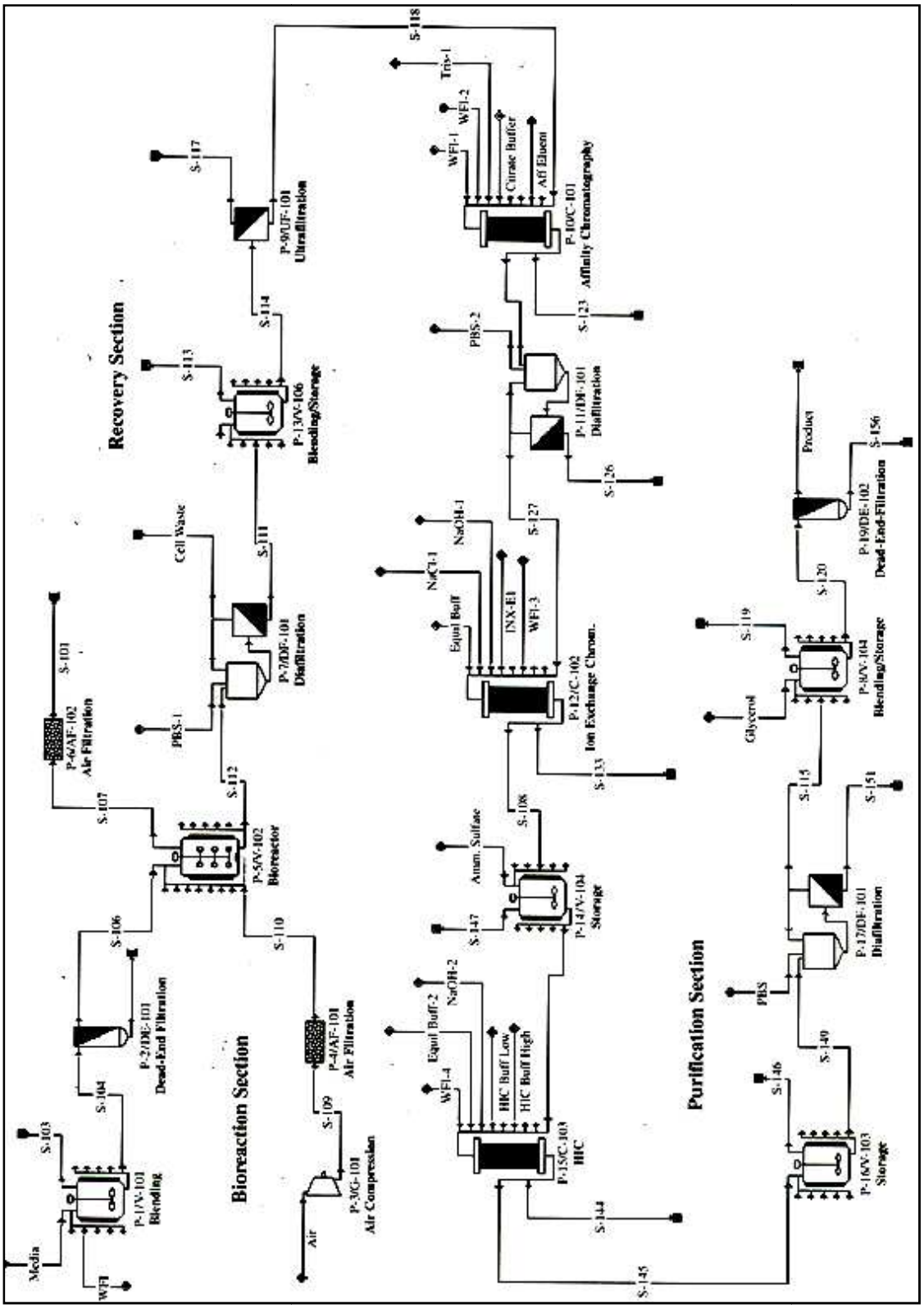

Figure 39: A flowsheet of a typical large-scale monoclonal antibody production

Source: Harrison, R. et al., *Bioseparations Science and Engineering* (2003), pg 362-367.

7.2 Large-scale Production of MAb-SWNT Conjugates

The large-scale production of the monoclonal antibody-single-walled carbon nanotube (mAb-SWNT) conjugates was based on a paper by Shao et al[8]. The values for this operation were also based on projected production of the mAb-SWNT conjugates for the population of breast cancer patients under the same assumptions as in the large-scale production of monoclonal antibodies. There are four main steps involved in this operation: preparation of SWNTs in phosphate buffered saline (PBS) solution, the surfactant addition to SWNTs, the preparation of the antibody solutions, and the mixing of the antibody solution and SWNT solution.

The SWNTs are assumed to be in bundles, and they are put through a bead mill to break up the bundles into individual carbon nanotubes. Following the bead milling, the SWNTs in PBS are centrifuged and mixed with a 1-pyrenebutanoyl/methanol solution to prepare the SWNTs for molecular attachment. Then the solution is mixed with poly(ethylene glycol) (PEG). PEG is used as the surfactant, where it forms a monolayer to prevent other molecules from attaching to the SWNTs. The antibody solutions are mixed with PBS and then sent to a blender, where they will be mixed with the functionalized SWNTs. Following incubation, the solution will be centrifuged to remove excess antibodies and to yield mAb-SWNT conjugates to be used for the cancer treatment. It is assumed that there will be a 1:1 ratio of monoclonal antibodies attaching to the SWNTs. A flowsheet of the large-scale process is illustrated in Figure 40.

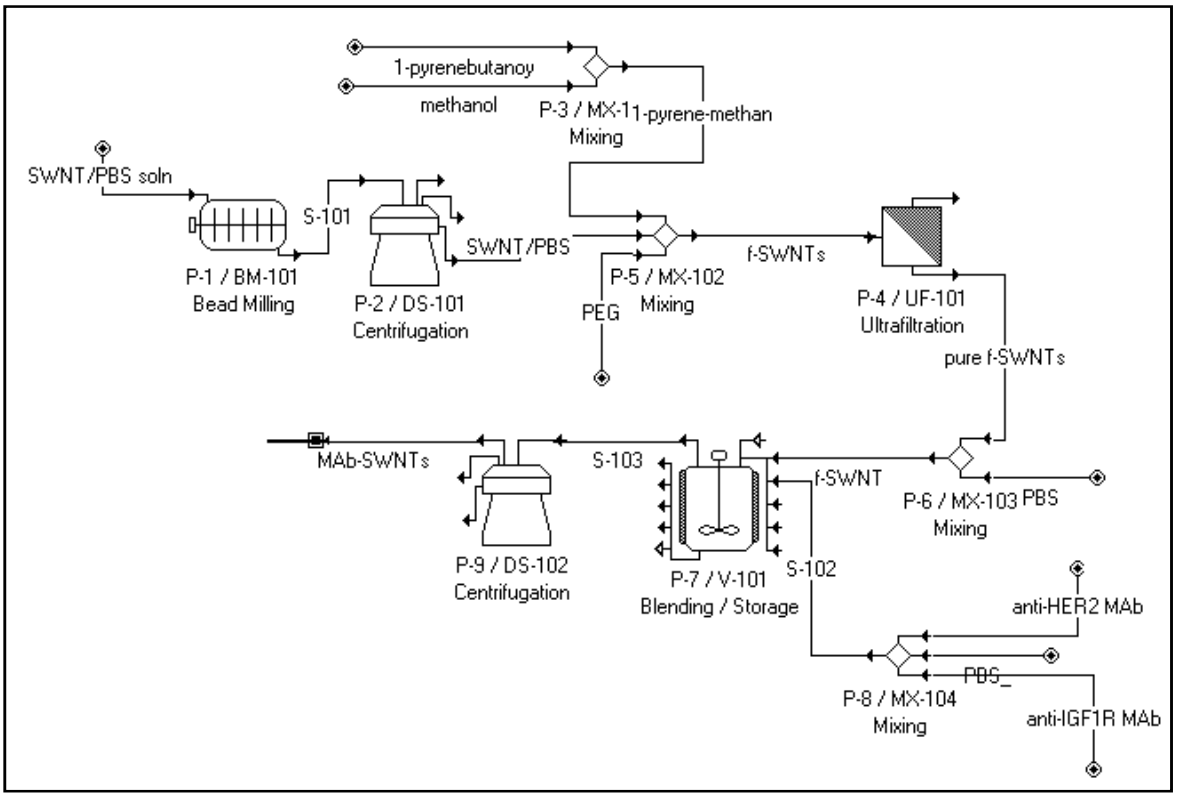

Figure 40: A flowsheet of the proposed monoclonal antibody-carbon nanotube conjugate production

8. Business Plan

The current business plan is to look towards pre-FDA testing. The company seeks to be in the forefront of breast cancer therapy with the novel treatment that is minimally invasive and more effective than current treatments.

8.1 Market Strategy

The market for the proposed treatment appears promising. Therapeutic monoclonal antibodies are a large trend in the biotechnology industry. It is expected that the global market for monoclonal antibodies will be $16.7 billion in 2008. Of the therapeutic categories, oncology is projected to be on top with earnings of $7.2 billion or 43% of the market share. The industry is expected to double the number of monoclonal antibody product approvals within the next few years[14]. The market for carbon nanotubes is currently small, but as more research is done on

these unique materials, more applications will be uncovered, and the market is expected to increase.

8.2 Breast Cancer Incidence in the US

In 2004, breast cancer affected about 500 out of every 100,000 women in the US[3]. At that time, the US population was 293 million people[15], which means there were about 1.5 million breast cancer sufferers in 2004. Using the US Census Bureau population data from the past several years, a line was extrapolated to estimate the number of breast cancer patients in 2008. The numbers are shown below in Table 4.

Race	Incidence (per 100,000) in 2004	Incidence (per 100,000) in 2008	Total projected incidence in 2008
White	132.5	137.5	418,102
African American	118.3	122.7	373,294
Asian	89.0	92.3	280,838
Hispanic	89.3	92.6	281,785
American Indian	69.8	72.4	220,253
Total			**1,574,272**

Table 4: Estimated breast cancer incidence in 2008

Source: *Population Division, U.S. Census Bureau (2007), http://www.census.gov/popest/states/NST-ann-est.html*

Thus, the number of US women suffering from breast cancer in 2008 is about 1.6 million.

8.3 Costs

Costs for the equipment necessary for large-scale monoclonal antibody production were estimated from Harrison et al. by using a multiplicative factor to account for the larger production rate than what was detailed in the literature[13]. The equipment cost of the large-scale monoclonal antibody production unit remains the most uncertain in the cost calculations. Because our output is much higher than the monoclonal antibody annual production, bigger equipment is needed and parallel operations should be considered in order to produce enough antibodies to serve all of the breast cancer patients in the US. The equipment costs for the large-scale mAb-SWNT attachment process were estimated based on the scaleup capacity.

The total capital investment was estimated as a percentage of the equipment cost using the factors in Peters et al[16]. The fixed capital investment for both the production and conjugation of monoclonal antibodies was determined to be $107 million, while the total capital investment was $128 million. The total product cost was determined to be $470 million or $760/gram. This includes raw materials, reagents, operating labor, and maintenance.

The minimum selling price was determined through the Solver function in Microsoft Excel. Assuming that equipment costs are ten times greater than estimated from Harrison et al., the mAb-SWNT drug would need to be sold at 1.8 times the total product cost (or $1340/g) in order to break even (i.e., in order for the net present worth to equal zero). If the selling price were set to twice the product cost, the net present value would be $542 million.

9. Conclusions

Mathematical models were successfully generated to predict

- the initial dosage requirement of the drug as a function of tumor volume
- the required time for NIR emission following injection
- the temperature gradient of the tumor cell during NIR radiation
- the ratio of dead tumor cells to total cells in a colony as a function of time
- the time required for a second irradiation based on a temperature profile immediately following the first irradiation

Graphs of the concentrations of mAb-SWNT for the tumors and surrounding tissue were generated based on the PBPK model. The point where the concentration of the mAb-SWNT is at a minimum for the normal cells is the optimal place to begin NIR irradiation.

Based on the simulation of the temperature gradient of the tumor, the damage to the surrounding normal tissue will be minimal due to the small amount of energy emitted from the NIR laser. Assuming that the critical temperature is 57°C, three minutes of irradiation is

sufficient to kill most of the tumors while curtailing negative effects to the surrounding tissue. The mAb-SWNT uptake by the normal cells due to its lower expression of HER2 and IGF1R recptors is assumed to be very small compared to the uptake by cancer cells. Additionally, the NIR laser is intended to only target the tumor area, so as to further minimize any damage to adjacent normal cells.

These models offer a customized, multifaceted approach to cancer therapy using monoclonal antibodies attached to carbon nanotubes. The parameters for the tumor volume, patient's weight, among other things unique to the patient, can be easily adjusted so that treatment can be offered more efficiently. By using mathematical models, we are providing the laboratory-tested cancer therapy a means to be more useful at the clinical level by considering the individuality of the patient.

10. Recommendations for Future Studies

Projects that have the potential to impact worldwide health can always be further studied. Recommendations for future studies include

- Exploration of FDA approval
- Studies of risk analysis
- Creation of an economic model that takes into account uncertainty
- Development of more accurate parameters for mAb catabolism to improve the mathematical models
- Development of a business plan
- Use of transgenic animals for animal testing
- Determination of the treatment cost per patient
- Use of SWNTs as multifunctional systems by attaching therapeutic and imaging molecules to target tumors

10.1 Single-walled Carbon Nanotube Dimensions

The length and diameter of the SWNTs were assumed to be constant; this does not describe the actual behaviors. In the future, an optimization procedure would need to be implemented to determine the most biologically favorable SWNT diameter and length for treatment. Once these values are known, then the optimal thermal energy for NIR emission can be determined. Under the optimized route, the number of SWNTs can be calculated and then compared to the numbers presented in this report.

11. References

1. American Cancer Society, http://www.cancer.org
2. US Mortality Public Use Data Tape 2003, National Center for Health Statistics, Centers for Disease Control and Prevention, 2006.
3. *Breast Cancer Facts and Figures 2007-2008*, American Cancer Society.
4. *Brock Biology of Microorganisms* (9th ed.), Madigan, M.T., Martinko, J.M., and Parker, J., Prentice-Hall, Inc., Upper Saddle River, New Jersey, 2000, 803-838.
5. Klumpp, C., Kostarelos, K., Prato, M., and Bianco, A., Functionalized carbon nanotubes as emerging nanovectors for the delivery of theraeutics, *Biochimica et Biophysica Acta* (2006), 1758(3):404-412.
6. Dresselhaus, M.S., Dresselhaus, G., Charlier, J.C., and Hernandez, C.E., Electronic, thermal, and mechanical properties of carbon nanotubes, *Philosophical Transactions: Mathematical, Physical, and Engineering Sciences* (2004), 362(1823):2065-2098.
7. Jiang, W., Kim, B., Rutka, J., and Chan, W., Advances and challenges of nanotechnology-based drug delivery systems, *Expert Opinion on Drug Delivery* (2007), 4(6): 621-633.
8. Shao, N., Lu, S., Wickstrom, E., and Panchapakesan, B., Integrated molecular targeting of IGF1T and HER2 surface receptors and destruction of breast cancer cells using single wall carbon nanotubes, *Nanotechnology* (2007), 18:1-9.
9. Britz, D. and Khlobystov, A., Noncovalent interactions of molecules with single walled carbon nanotubes, *Chemical Society Reviews* (2006), 35:637-659.
10. Helland, A., Wick, P., Koehler, A., Schmid, K., and Som, C., Reviewing the environmental and human health knowledge base of carbon nanotubes, *Environmental Health Perspectives* (2007), 115(8):1125-1131.
11. Bianco, A., Kostarelos, K., Partidos, C., and Prato, M., Biomedical applications of functionalised carbon nanotubes, *Chemical Communications* (2005), 571-577.
12. Singh, R., Pantarotto, D., Lacerda, L., Pastorin, G., Klumpp, C., Prato, M., Bianco, A., and Kostarelos, K., Tissue biodistribution and blood clearance rates of intravenously

administered carbon nanotube radiotracers, *Proceedings of the National Academy of Sciences* (2006), 103(9):3357-3362.

13. Harrison, R., Todd, P., Rudge, S., and Petrides, D., *Bioseparations Science and Engineering* (2003), pg 362-367.
14. Reichert, J. and Pavlou, A., Monoclonal antibodies market, *Nature Reviews* (2004), 3:383-384.
15. Population Division, U.S. Census Bureau (2007), <http://www.census.gov/popest/states/NST-ann-est.html>
16. Peters, M., Timmerhaus, K., and West, R., *Plant Design and Economics for Chemical Engineers* (2003), 251-253.
17. Partridge, A., Burstein, H., and Winer, E., Side effects of chemotherapy and combined chemohormonal therapy in women with early-stage breast cancer, *Journal of the National Cancer Institute Monographs*, 30:135-142.
18. Chang-Claude, J., Popanda, O., Tan, X., Kropp, S., Helmbold, I., von Fournier, D., Haase, W., Sautter-Bihl, M., Wenz, F., Schmezer, P., and Ambrosone, C., Association between polymorphisms in the DNA repair genes, XRCC1, APE1, and XPD and acute side effects of radiotherapy in breast cancer patients, *Clinical Cancer Research* (2005), 11(13):4802-4809.
19. Klefstrom, P., Grohn, P., Heinonen, E., Holsti, L., and Holsti, P., Adjuvant postoperative radiotherapy, chemotherapy, and immunotherapy in stage III breast cancer, *Cancer*, 60(5):936-942.
20. Vogel, C. and Franco, S., Clinical experience with TrastuzumAb (Herceptin), *The Breast Journal* (2003), 9(6):452-462.
21. Levine, M., TrastuzumAb cardiac side effects: only time will tell (2005), *Journal of Clinical Oncology*, 23(31)7775-7776.
22. Thomas, G., Chappell,M., Dykes, P., Ramsden, D., Godfrey, K., Ellis, J., and Bradwell, A., Effect of dose, molecular Size, affinity, and protein binding on tumor uptake of antibody of ligand: A biomathematical model, *Cancer Research* (1989), 49:3290-3296.

23. Chappell, M., Thomas, G., Godfrey, K., and Bradwell, A., Optimal Tumor Targeting by Antibodies: Development of a Mathematical Model, *Journal of Pharmacokinetics and Biopharmaceutics* (1991), 227-260.
24. Prlic, M. and Bevan, M., An Antibody Paradox, Resolved, *Science* (March 31, 2006), 1875-1876.
25. Kam, N., O'Connell, M., Wisdom, J., Dai, H., and Gray, H., Carbon Nanotubes as Multifunctional Biological Transporters and Near-Infrared Agents for Selective Cancer Cell Destruction, *Proceedings of the National Academy of Sciences* (2005), 11600-11605.
26. Joris, I., Tumors, Cells, *Tissues, and Disease : Principles of General Pathology* (2004), 789.
27. Meyskens, F., Thomson, S., Moon, T., Quantitation of the Number of Cells within Tumor Colonies in Semisolid Medium and Their Growth as Oblate Spheroids, *CANCER RESEARCH* 1984, 271-277.
28. Kuszyk, B., Corl, F., Franano, F., Bluemke, D., Lawrence, V., Fortman, B.,; Fishman, E., Tumor Transport Physiology: Implications for Imaging and Imanging-Guided Therapy, American Roentgen Ray Society (2001), 747-753.
29. Meibohm, B., Pharmacokinetics of Monocloanal Antibodies, *Pharmacokinetics and Pharmacodynamics of Biotech Drugs: Principles and Case Studies* (2001), 71.
30. Shimizu, C., Hasegawa, T., Tani, Y., Takahashi, F., Takeuchi, M., Watanabe, T., Ando, M., Katsumata, N., Fujiwara, Y., Expression of insulin-like growth factor 1 receptor in primary breast cancer: immunohistochemical analysis, *Human Pathology* (2004), 35(12): 1537-1542.
31. Tian, X., Aruva, M. R., Qin, W., Zhu, W., Sauter, E. R., Thakur, M. L., Wickstrom, E., Noninvasive molecular imaging of *MYC* mRNA expression in human breast cancer xenografts with a [^{99m}Tc]peptide-peptide nucleic acid-peptide chimera, *Bioconjugate Chemistry* (2005), 16(1):70-79.
32. Bartucci, M., Morelli, C., Mauro, L., Ando, S., and Surmacz, E., Differential insulin-like growth factor I receptor signaling and function in estrogen receptor (ER)-positive MCF-7 and ER-negative MDA-MB-231 breast cancer cells., *Cancer Research* (2001), 61:6747–6754.
33. Peyrat, J.P., Bonneterre, J., Vennin, P.H., Jammes, R., Beuscart, R., Hecquet, B., Djiane, J., Lefebvre, J., and Demaille, A., Insulin-like growth factor 1 receptors (IGF1-R) and IGF in

human breast tumors, *Journal of Steroid and Biochemistry and Molecular Biology* (1990), 37(6):823-827.

34. Nahta, R., Yu, D., Hung, M., Hortobagyi, G.N., and Esteva, F.J., Mechanisms of disease: understanding resistance to HER2-targeted therapy in human breast cancer, *Nature* (2006), 3(5):269-280.
35. Ross, J.S., Fletcher, J.A., Bloom, K.J., Linette, G.P., Stec, J., Symmans, W.F., Pusztai, L., and Hortobagyi, G.N., Targeted therapy in breast cancer, *Molecular & Cellular Proteomics* (2004) 3:379-398.
36. Ferl, G.Z., Wu, A.M., Distefano III, J.J., A predictive model of therapeutic monoclonal antibody dynamics and regulation by the neonatal Fc receptor (FcRn)., *Annals of Biomedical Engineering* (2005), 33(11):1640–1652.
37. Rippe B., Haraldsson B., Transport of macromolecules across microvascular walls: the two-pore theory. *Physiological Reviews* (1994), 74(1):163-219.
38. Kargol, A., Przestalski, M., and Kargol, M., A study of porous structure of cellular membranes, *Cryobiology* (2005) 50:332–337.
39. Davda, J.P., Jain, M., Batra, S.K., A physiologically based pharmacokinetic (PBPK) model to characterize and predict the disposition of monoclonal antibody CC49 and its single chain Fv constructs, *International Immunopharmacology* (2008), 8(3):401-413.
40. Cengel, Y.A*., Heat and Mass Transfer: A Practical Approach* 3rd Edition., Mc Graw Hill, 2007, 313.
41. Hughes, G., Nanostructure-mediated drug delivery, *Nanomedicine: Nanotechnology, Biology, and Medicine I* (2005), 22-30.

12. Appendix A - PBPK Model Parameters

Organ/Tissue	Blood flow rate Q (ml/h)	Vascular volume Vv (ml)	Interstitial volume Vi (ml)	Total volume Vt (ml)	Partition coefficient Rc	Lymph flow rate L (ml/h/g)	Fluid recirculation rate J_{iso} (ml/h/g)
Blood	3.36E+05	5200		5200	1		
Lung	3.36E+05	66.5	199.5	999	0.298	4.30E-02	0.14
Heart	1.44E+04	24.5	66.5	300	0.143	4.30E-03	0.3
Kidney	7.44E+04	105	353.5	284	0.339	7.40E-02	0.23
Liver	8.70E+04	350	875	1809	0.263	8.70E-02	0.71
Spleen	4.62E+03	35	70	173.4	0.2	8.70E-04	0.47
Tumor	6.10E+01	1.4	10	15	0.38	3.00E-02	0.047
Rest of Body	1.56E+05	5862	12477.5	61215	0.213	0.1101	0.75

Organ/Tissue	Permeability-surface		Catabolism rate k_{cat} ($h^{-}1$)	Catabolite clearance CL (ml/h)	Mass (g)
	PS_L (ml/h/g)	PS_S (ml/h/g)			
Blood					1445.974
Lung	2.08E-05	6.08E-05	3.40E-02	2.50E-02	3.63E+02
Heart	2.08E-05	6.08E-05	2.60E-02	1.10E-02	2.54E+02
Kidney	2.08E-05	6.08E-05	1.00E-03	0.00E+00	5.68E+02
Liver	2.08E-04	6.08E-04	8.20E-09	4.70E-02	1.81E+03
Spleen	2.08E-04	6.08E-04	9.40E-04	7.80E-03	1.91E+02
Tumor	1.63E-04	5.95E-04	5.30E-04	7.40E-04	2.00E+01
Rest of Body	2.08E-05	6.08E-05	4.40E-06	4.00E-03	3.16E+04

Estimating the interstitial, and vascular volume of tumor				
Vt (ml)	$V_{interstitial}$	$V_{vascular}$	Ratio,V_i	Ratio, V_v
20	10	1.4	0.5	0.07
10	0	52000		
15	0	78000		
25	0	130000		

Tumor antigen conc. B_{max} (M)	5.62E-07
Osmotic reflection coefficients	
σ_L	0.1
σ_S	0.74
Specific binding rate constants	
k_{fag} ($M^{-1}h^{-1}$)	7.92E+08
k_{rag} (h^{-1})	7.45
Rate constants for between FcRn&IgG	
k_{int} (h^{-1})	9.26E-06
k_{rec} (h^{-1})	0.26
Two-pore model parameters	
α_L	0.242
α_S	0.758
Excretion rate, U (ml/h)	27.475

Table 5. The rate constant variables

13. Appendix B – Binding Kinetics Model

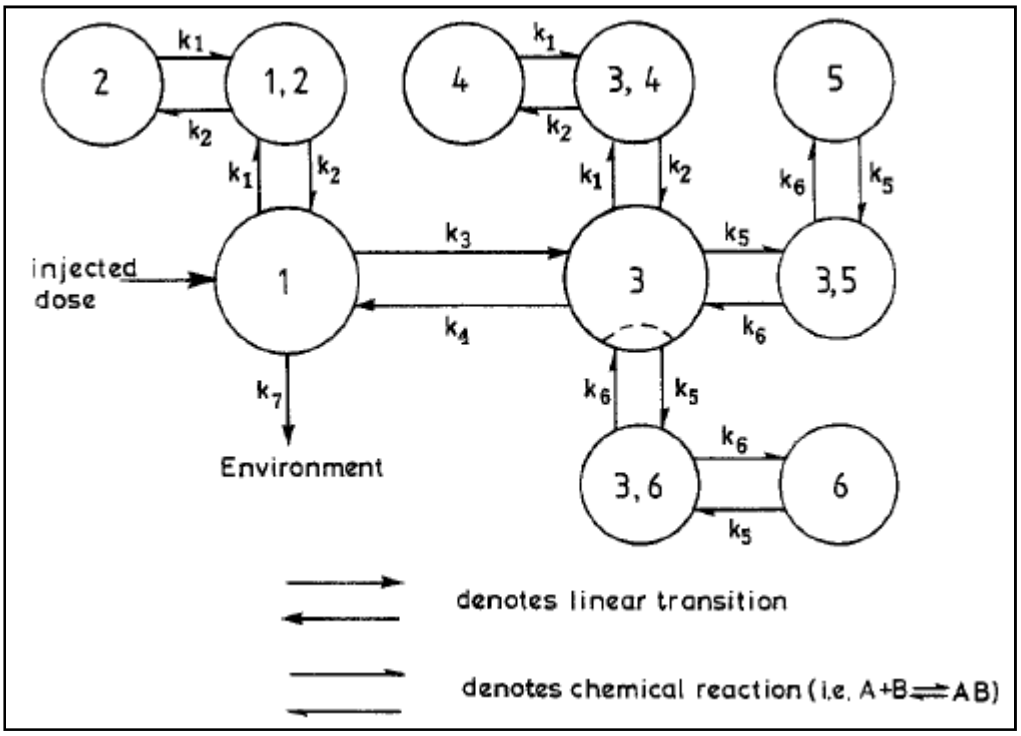

Figure 41: The compartmental model of the system

Figure 19 is same compartmental model of the system in Figure 9 but with different numbers. Table 6 lists the values of rate constants *k* found from different literatures.

k_1	Rate constant of association for protein binding	10^4 ~ 10^8 $mol^{-1}s^{-1}$
k_2	Rate constant of dissociation for protein binding	10^{-2} ~ 10^2 s^{-1}
k_3	Rate constant of transfer from plasma to ECF	10^{-2} ~ 10^{-5} s^{-1}
k_4	Rate constant of transfer from ECF to plasma	2×10^{-3} ~ 2×10^{-6} s^{-1}
k_5	Rate constant of association to specific binding site	10^5 ~ 10^9 $mol^{-1}s^{-1}$
k_6	Rate constant of dissociation from specific binding site	10^{-1} ~ 10^{-6} s^{-1}
k_7	Rate constant of transfer from plasma to environment	10^{-2} ~ 10^{-5} s^{-1}

Table 6. The rate constant variables (Gillian D. Thomas, 1989)

All of the values were experimentally obtained. One of the major tasks in the preclinical phase for the FDA-approved process will be to obtain more accurate values of the rate constant. Every individual has a unique metabolism rate. The treatment should be done by carefully verifying the constants to predict the distribution of the drugs.

There are six differential ordinary equations which can describe the system as follows:

$$\frac{dq_1}{dt} = k_4 q_3 - (k_3 + k_7) q_1 + k_2 q_1 q_2 \quad \textbf{Equation 23}$$

$$\frac{dq_{1,2}}{dt} = k_1 q_1 q_2 - k_2 q_{1,2} \quad \textbf{Equation 24}$$

$$\frac{dq_3}{dt} = k_3 q_1 - k_4 q_3 - k_1 q_3 q_4 + k_2 q_{3,4} - k_5 q_3 q_5 + k_6 q_{3,5} - k_5 (\frac{5V_{3,6}}{V_3}) q_3 q_6 + k_6 q_{3,6} \quad \textbf{Equation 25}$$

$$\frac{dq_{3,4}}{dt} = k_1 q_3 q_4 - k_2 q_{3,4} \quad \textbf{Equation 26}$$

$$\frac{dq_{3,5}}{dt} = k_5 q_3 q_5 - k_6 q_{3,5} \quad \textbf{Equation 27}$$

$$\frac{dq_{3,6}}{dt} = k_5 (\frac{5V_{3,6}}{V_3}) q_3 q_6 - k_6 q_{3,6} \quad \textbf{Equation 28}$$

where q_i is the amount of unbounded substance in compartment $_i$, and $q_{i,j}$ is the amount of bounded substance in the compartment $_{i,j}$ out from compartment $_i$ in the unit moles. It was found that the amount of the bounded substance transferred from ECF to tumors is relatively small compared to the amount of the substances in ECF. In order to explain this observation from the experiments, the assumption was made that the substance in tumor $q_{3,6}$ only receives the substances from a fraction of the total amount in ECF, q_3 (Michael J. Chappell, 1991). Based on the law of the conservation, the concentration in the unbounded substance in Compartments 2, 4, 5, and 6 can be expressed as

$$\boldsymbol{x_2 = PP - x_{1,2}} \quad \textbf{Equation 29}$$

$$\boldsymbol{x_4 = PE - x_{3,4}} \qquad \textbf{Equation 30}$$

$$\boldsymbol{x_5 = R - x_{3,5}} \qquad \textbf{Equation 31}$$

$$\boldsymbol{x_6 = S - x_{3,6}} \qquad \textbf{Equation 32}$$

where x_i is the concentration of the unbound substance in the compartment i. By substituting Equations 15 through 18 into Equations 9 through 14, the compartment 2,4,5, and 6 can be made as pseudo compartment followed by,

$$\frac{dq_1}{dt} = k_4 q_3 - (k_3 + k_7) q_1 + k_2 q_1 (PP \cdot V1 - q_{1,2}) \qquad \textbf{Equation 33}$$

$$\frac{dq_{1,2}}{dt} = k_1 q_1 (PP \cdot V1 - q_{1,2}) - k_2 q_{1,2} \qquad \textbf{Equation 34}$$

$$\frac{dq_3}{dt} = k_3 q_1 - k_4 q_3 - k_1 q_3 (PE \cdot V3 - q_{3,4}) + k_2 q_{3,4} - k_5 q_3 (R \cdot V3 - q_{3,5}) + k_6 q_{3,5} - k_5 (\frac{5 \cdot V_{3,6}}{V_3}) q_3 (S \cdot V3{,}6 - q_{3,6}) + k_6 q_{3,6} \qquad \textbf{Equation 35}$$

$$\frac{dq_{3,4}}{dt} = k_1 q_3 (PE \cdot V3 - q_{3,4}) - k_2 q_{3,4} \qquad \textbf{Equation 36}$$

$$\frac{dq_{3,5}}{dt} = k_5 q_3 (R \cdot V3 - q_{3,5}) - k_6 q_{3,5} \qquad \textbf{Equation 37}$$

$$\frac{dq_{3,6}}{dt} = k_5 (\frac{5 \cdot V_{3,6}}{V_3}) q_3 (S \cdot V3{,}6 - q_{3,6}) - k_6 q_{3,6} \qquad \textbf{Equation 38}$$

Other variables and parameters are shown on Table 7.

V_1	Volume of plasma	2.5 L
V_3	Volume of ECF	12 L
$V_{3,6}$	Volume of tumor	10^{-2} ~ 2.5×10^{-2} L
PP	Concentration of plasma protein binding sites	10^{-3} ~ 10^{-6} M L^{-1}
PE	Concentration of ECF protein binding sites	10^{-3} ~ 10^{-6} M L^{-1}
R	Concentration of specific binding sites on normal tissue in ECF	2×10^{-10} M L^{-1}
S	Concentration of specific binding sites on tumor	2×10^{-8} M L^{-1}
D	Initial dose	6×10^{-10} ~ 6×10^{-7} moles

Table 7: Variables for solving differential equations

Tumors are only able to bind to the substances if the substances are located in the tumors' reachable vicinity. The estimated value of the region to which the tumor can attract the substance is approximately five times of the tumor volume. Tumor cells are able to absorb more substance than other normal cells due to abnormal growth. The tumors are striving to expand the capillary permeability in order to satisfy the nutrient and oxygen demands as the sizes of tumor cells are growing. Therefore this estimation is reasonable. In addition, there are other assumptions needed for this system; the binding proteins and tissue in ECF can absorb the substance in a uniform manner.

The rate constants are varied from10^{-5} to 10^{9}. The maximum stiffness factor is 10^{14}. The wide range of k values makes very stiff differential equations. The Runge-Kutta-Gill method, which is commonly used, is not desirable to solve the very stiff differential equations (David Garfinkel, 1977). Polymath software ver. 6.1 was used to solve the stiff differential equations. The software provides a stiff differential equations algorithm to allow users to set up the smallest step size to avoid the computational miscalculations. Polymath is able to deal with the stiff differential equations in the maximum stiffness factor of 10^{11}. The stability is determined by the empirical values on a case-by-case basis (David Garfinkel, 1977). Therefore the rate constants need to be adjusted so that the Polymath software can calculate the stiff differential equations.

14. Appendix C – Equations used in the PBPK Model

The equations below are taken from Davda, J.P. et al[39] and describe the transport and tissue disposition of monoclonal antibodies.

For blood:

For IgG

$$V_B \frac{dC_B}{dt} = (Q_{LU} - L_{LU})C_{v,LU} + L_{LU}C_{i,LU} + L_{LI}C_{i,LI} + L_{SP}C_{i,SP} + L_K C_{i,K} + L_T C_{i,T} + L_H C_{i,H} + L_{RB}C_{i,RB} - (Q_{LI} - L_{SP} + Q_K - Q_T + Q_H - Q_{RB})C_B$$

For catabolite pool in blood

$$V_B \frac{dC_{m,B}}{dt} = CL_T C_{m,T} + CL_{LI}C_{m,LI} + CL_{SP}C_{m,SP} + CL_H C_{m,H} + CL_{RB}C_{m,RB} + CL_{LU}C_{m,LU} + Q_K L_{M,K}$$

mAb concentration in blood

$$C_{TOT,B} = C_B + C_{m,B}$$

For lung:

For vascular space

$$V_{v,LU} \frac{dC_{v,LU}}{dt} = (Q_{LI} - L_{LI})C_{v,LI} + (Q_K - L_K)C_{v,K} + (Q_T - L_T)C_{v,T} + (Q_H - L_H)C_{v,H} + (Q_{RB} - L_{RB})C_{v,RB} + (Q_{LU} - L_{LU})C_{v,LU} - k_{cat,LU}C_{v,LU}V_{v,LU} - J_{L,LU}(1 - \sigma_L)C_{v,LU} - PS_{L,LU}\left(C_{v,LU} - \frac{C_{i,LU}}{R_{LU}}\right)\frac{Pe_{L,LU}}{e^{Pe_{s,LU}} - 1} - J_{S,LU}(1 - \sigma_S)C_{v,LU} - PS_{S,LU}\left(C_{v,LU} - \frac{C_{i,LU}}{R_{LU}}\right)\frac{Pe_{S,LU}}{e^{Pe_{s,LU}} - 1}$$

For interstitial space

$$V_{i,LU}\frac{dC_{i,LU}}{dt} = J_{L,LU}(1-\sigma_L)C_{v,LU} - PS_{L,LU}\left(C_{v,LU} - \frac{C_{i,LU}}{R_{LU}}\right)\frac{Pe_{L,LU}}{e^{Pe_{s,LU}}-1} - J_{S,LU}(1-\sigma_S)C_{v,LU} - PS_{S,LU}\left(C_{v,LU} - \frac{C_{i,LU}}{R_{LU}}\right)\frac{Pe_{S,LU}}{e^{Pe_{s,LU}}-1} - L_{LU}C_{i,LU}$$

For catabolites

$$V_{v,LU}\frac{dC_{m,LU}}{dt} = k_{cat,LU}C_{v,LU}V_{v,LU} - CL_{LU}C_{m,LU}$$

mAb concentration in the lung

$$C_{TOT,LU} = \frac{(C_{v,LU} + C_{m,LU})V_{v,LU} + C_{i,LU}V_{i,LU}}{V_{LU}}$$

<u>For liver:</u>

For vascular space

$$V_{v,LI}\frac{dC_{v,LI}}{dt} = (Q_{SP} - L_{SP})C_{v,SP} + (Q_{LI} - Q_{SP} - L_{SP})C_B + k_{ree}C_{end,LI}V_{v,LI} + k_{int}C_{v,Li}V_{v,LI} - (Q_{LI} - L_{LI})C_{v,LI} - J_{L,LI}(1-\sigma_L)C_{v,LI} - PS_{L,LI}\left(C_{v,LI} - \frac{C_{i,LI}}{R_{LI}}\right)\frac{Pe_{L,LI}}{e^{Pe_{s,LI}}-1} - J_{S,LI}(1-\sigma_S)C_{v,LI} - PS_{S,LI}\left(C_{v,LI} - \frac{C_{i,LI}}{R_{LI}}\right)\frac{Pe_{S,LI}}{e^{Pe_{s,LI}}-1}$$

For interstitial space

$$V_{i,LI}\frac{dC_{i,LI}}{dt} = J_{L,LI}(1-\sigma_L)C_{v,LI} + PS_{L,LI}\left(C_{v,LI} - \frac{C_{i,LI}}{R_{LI}}\right)\frac{Pe_{L,LI}}{e^{Pe_{s,LI}}-1} + J_{S,LI}(1-\sigma_S)C_{v,LI} - PS_{S,LI}\left(C_{v,LI} - \frac{C_{i,LI}}{R_{LI}}\right)\frac{Pe_{S,LI}}{e^{Pe_{s,LI}}-1} - L_{LI}C_{i,LI}$$

For endosomal space

$$V_{v,LU}\frac{dC_{end,LI}}{dt} = k_{int}C_{v,LI}V_{v,LI} - k_{rec}C_{end,LI}V_{v,LI} - k_{cat,LI}CL_{LI}VC_{v,LI}$$

For catabolites

$$V_{v,LI}\frac{dC_{m,LI}}{dt} = k_{cat,LI}C_{v,LI}V_{v,LI} - CL_{LI}C_{m,LI}$$

mAb concentration in the liver

$$C_{TOT,LI} = \frac{(C_{v,LI} + C_{end,LI} + C_{m,LI})V_{v,LI} + C_{i,LI}V_{i,LI}}{V_{LI}}$$

<u>For spleen:</u>

For vascular space

$$\begin{aligned} V_{v,SP}\frac{dC_{v,SP}}{dt} = {} & Q_{SP}C_B - (Q_{SP} - L_{SP})C_{v,SP} + k_{cat,SP}C_{v,SP}V_{v,SP} - J_{L,SP}(1-\sigma_L)C_{v,SP} \\ & - PS_{L,SP}\left(C_{v,SP} - \frac{C_{i,SP}}{R_{SP}}\right)\frac{Pe_{L,SP}}{e^{Pe_{s,SP}} - 1} - J_{S,SP}(1-\sigma_S)C_{v,SP} \\ & - PS_{S,SP}\left(C_{v,SP} - \frac{C_{i,SP}}{R_{SP}}\right)\frac{Pe_{S,SP}}{e^{Pe_{s,SP}} - 1} \end{aligned}$$

For interstitial space

$$\begin{aligned} V_{i,SP}\frac{dC_{i,SP}}{dt} = {} & J_{L,SP}(1-\sigma_L)C_{v,SP} + PS_{L,SP}\left(C_{vSP} - \frac{C_{i,SP}}{R_{SP}}\right)\frac{Pe_{L,SP}}{e^{Pe_{s,SP}} - 1} + J_{S,SP}(1-\sigma_S)C_{v,SP} \\ & + PS_{S,SP}\left(C_{v,SP} - \frac{C_{i,SP}}{R_{SP}}\right)\frac{Pe_{S,SP}}{e^{Pe_{s,SP}} - 1} - L_{SP}C_{i,SP} \end{aligned}$$

For catabolites

$$V_{v,SP}\frac{dC_{m,SP}}{dt} = k_{cat,SP}C_{v,SP}V_{v,SP} - CL_{SP}C_{m,SP}$$

mAb concentration in the spleen

$$C_{TOT,SP} = \frac{(C_{v,SP} + C_{m,SP})V_{v,SP} + C_{i,SP}V_{i,SP}}{V_{SP}}$$

For tumor:

For vascular space

$$V_{v,T}\frac{dC_{v,T}}{dt} = Q_T C_B - (Q_T - L_T)C_{v,T} - J_{L,T}(1-\sigma_L)C_{v,T} - PS_{L,T}\left(C_{v,T} - \frac{C_{i,T}^f}{R_T}\right)\frac{Pe_{S,T}}{e^{Pe_{s,T}} - 1}$$
$$- J_{S,T}(1-\sigma_S)C_{v,T} - PS_{S,T}\left(C_{v,T} - \frac{C_{i,T}^f}{R_T}\right)\frac{Pe_{S,T}}{e^{Pe_{s,T}} - 1}$$

For free antibody concentration in the interstitial space

$$V_{i,T}\frac{dC_{i,T}^f}{dt} = J_{L,T}(1-\sigma_L)C_{v,T} + PS_{L,T}\left(C_{v,T} - \frac{C_{i,T}^f}{R_T}\right)\frac{Pe_{S,T}}{e^{Pe_{s,T}} - 1} + J_{S,T}(1-\sigma_S)C_{v,T}$$
$$+ PS_{S,T}\left(C_{v,T} - \frac{C_{i,T}^f}{R_T}\right)\frac{Pe_{S,T}}{e^{Pe_{s,T}} - 1} - k_{ag}^f C_{i,T}^f (B_{max} - C_{i,ag}^b)V_{i,T} + k_{ag}^r C_{i,ag}^b V_{i,T} - L_T C_{i,T}^f$$

For bound antibody concentration in the interstitial space

$$V_{i,T}\frac{dC_{i,ag}^b}{dt} = k_{ag}^f C_{i,T}^f (B_{max} - C_{i,ag}^b)V_{i,T} - k_{ag}^r C_{i,ag}^b V_{i,T} - k_{cat,ag} C_{i,ag}^b V_{i,T}$$

For catabolites

$$V_{i,T}\frac{dC_{m,T}}{dt} = k_{cat,ag} C_{v,T} V_{i,T} - CL_T C_{m,T}$$

mAb concentration in the tumor

$$C_{TOT,T} = \frac{(C_{i,T}^f + C_{i,ag}^b + C_{m,T})V_{v,T} + C_{v,T}V_{i,T}}{V_T}$$

For kidney:

For vascular space

$$V_{v,K}\frac{dC_{v,K}}{dt} = Q_K C_B - (Q_K - L_K)C_{v,K} - k_{cat,K}C_{v,K}V_{v,K} - J_{L,K}(1-\sigma_L)C_{v,K} - PS_{L,K}\left(C_{v,K} - \frac{C_{i,K}}{R_K}\right)\frac{Pe_{L,K}}{e^{Pe_{s,K}}-1} - J_{S,K}(1-\sigma_S)C_{v,K} - PS_{S,K}\left(C_{v,K} - \frac{C_{i,K}}{R_K}\right)\frac{Pe_{S,K}}{e^{Pe_{s,K}}-1}$$

For interstitial space

$$V_{i,K}\frac{dC_{i,K}}{dt} = J_{L,K}(1-\sigma_L)C_{v,K} + PS_{L,K}\left(C_{v,K} - \frac{C_{i,K}}{R_K}\right)\frac{Pe_{L,K}}{e^{Pe_{s,K}}-1} + J_{S,K}(1-\sigma_S)C_{v,K} + PS_{S,K}\left(C_{v,K} - \frac{C_{i,K}}{R_K}\right)\frac{Pe_{S,K}}{e^{Pe_{s,K}}-1} - L_K C_{i,K}$$

For catabolites

$$V_{v,K}\frac{dC_{m,K}}{dt} = k_{cat,K}C_{v,K}V_{v,K} - Q_K C_{m,B} - UC_{m,K}V_{v,K}$$

mAb concentration in the kidney

$$C_{TOT,K} = \frac{(C_{v,K} + C_{m,K})V_{v,K} + C_{i,K}V_{i,K}}{V_K}$$

For heart:

For vascular space

$$V_{v,H}\frac{dC_{v,H}}{dt} = Q_H C_B - (Q_H - L_H)C_{v,H} - k_{cat,H}C_{v,H}V_{v,H} - J_{L,H}(1-\sigma_L)C_{v,H} - PS_{L,H}\left(C_{v,H} - \frac{C_{i,H}}{R_H}\right)\frac{Pe_{L,H}}{e^{Pe_{s,H}}-1} - J_{S,H}(1-\sigma_S)C_{v,H} - PS_{S,H}\left(C_{v,H} - \frac{C_{i,H}}{R_H}\right)\frac{Pe_{S,H}}{e^{Pe_{s,H}}-1}$$

For interstitial space

$$V_{i,H}\frac{dC_{i,H}}{dt} = J_{L,H}(1-\sigma_L)C_{v,H} + PS_{L,H}\left(C_{v,H} - \frac{C_{i,H}}{R_H}\right)\frac{Pe_{L,H}}{e^{Pe_{s,H}}-1} + J_{S,H}(1-\sigma_S)C_{v,H} + PS_{S,H}\left(C_{v,H} - \frac{C_{i,H}}{R_H}\right)\frac{Pe_{S,H}}{e^{Pe_{s,H}}-1} - L_H C_{i,H}$$

For catabolites

$$V_{v,H}\frac{dC_{m,H}}{dt} = k_{cat,H}C_{v,H}V_{v,H} - CL_H C_{m,H}$$

mAb concentration in the heart

$$C_{TOT,H} = \frac{(C_{v,H} + C_{m,H})V_{v,H} + C_{i,H}V_{i,H}}{V_H}$$

<u>For the rest of the body:</u>

For vascular space

$$V_{v,RB}\frac{dC_{v,RB}}{dt} = Q_{RB}C_B - (Q_{RB} - L_{RB})C_{v,RB} + k_{red}C_{end,RB}V_{v,RB} - k_{int}C_{v,RB}V_{v,RB} - J_{L,RB}(1-\sigma_L)C_{v,RB} - PS_{L,RB}\left(C_{v,RB} - \frac{C_{i,RB}}{R_{RB}}\right)\frac{Pe_{L,RB}}{e^{Pe_{s,RB}}-1} - J_{S,RB}(1-\sigma_S)C_{v,RB} - PS_{S,RB}\left(C_{v,H} - \frac{C_{i,RB}}{R_{RB}}\right)\frac{Pe_{S,RB}}{e^{Pe_{s,RB}}-1}$$

For interstitial space

$$V_{i,RB}\frac{dC_{i,RB}}{dt} = J_{L,RB}(1-\sigma_L)C_{v,RB} + PS_{L,RB}\left(C_{v,RB} - \frac{C_{i,RB}}{R_{RB}}\right)\frac{Pe_{L,RB}}{e^{Pe_{s,RB}}-1} + J_{S,RB}(1-\sigma_S)C_{v,RB} + PS_{S,RB}\left(C_{v,H} - \frac{C_{i,RB}}{R_{RB}}\right)\frac{Pe_{S,RB}}{e^{Pe_{s,RB}}-1} - L_{RB}C_{i,RB}$$

For endosomal space

$$V_{v,RB}\frac{dC_{end,RB}}{dt} = k_{int}C_{v,RB}V_{v,RB} - k_{rec}C_{end,RB}V_{v,RB} - k_{cat,RB}C_{end,RB}V_{v,RB}$$

For catabolites

$$V_{v,RB}\frac{dC_{m,RB}}{dt} = k_{cat,RB}C_{end,RB}V_{v,RB} - CL_{RB}C_{m,RB}$$

mAb concentration in the rest of the body

$$C_{TOT,RB} = \frac{\left(C_{v,RB} + C_{end,RB} + C_{m,RB}\right)V_{v,RB} + C_{i,RB}V_{i,RB}}{V_{RB}}$$

15. Appendix D – Random Number Method

D_{cells} were generated randomly by using random function in Excel program with the range between 50 and 200 µm. N_{cells} were calculated using Equation 11 with the 1500 of random numbers D_{cells}. The histogram of N_{cells} calculated by 1500 random numbers of D_{cells} were plotted.

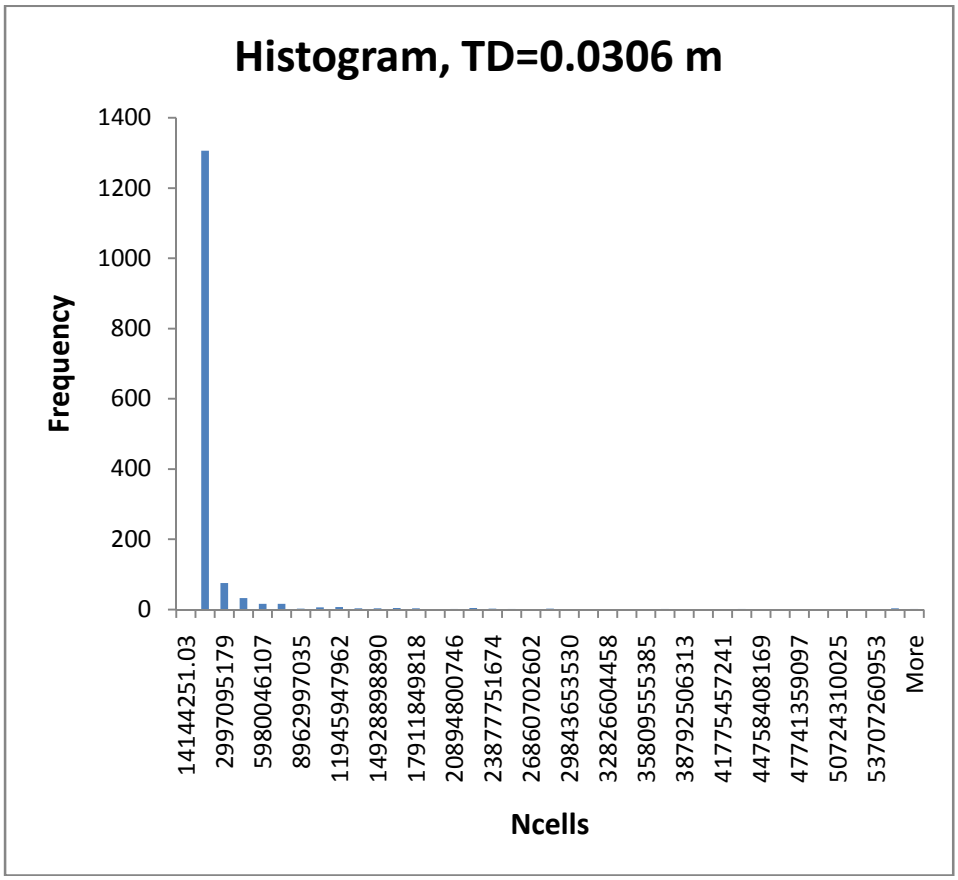

Figure 42: Histogram of N_{cells} values with the tumor diameter of 0.0306 m

Figure 20 shows that most of N_{cells} with the tumor diameter of 0.0306 m are distributed on 1.51×10^{9}. Therefore, it can be safely assumed that the number of cells inside of the tumor colony is 1.51×10^{9}. In a same method, N_{cells} with different tumor diameter can also be determined. N_{cells} with the tumor diameter of 0.0337m and 0.03627m can be found 1.89×10^{9} and 2.26×10^{9} respectively.

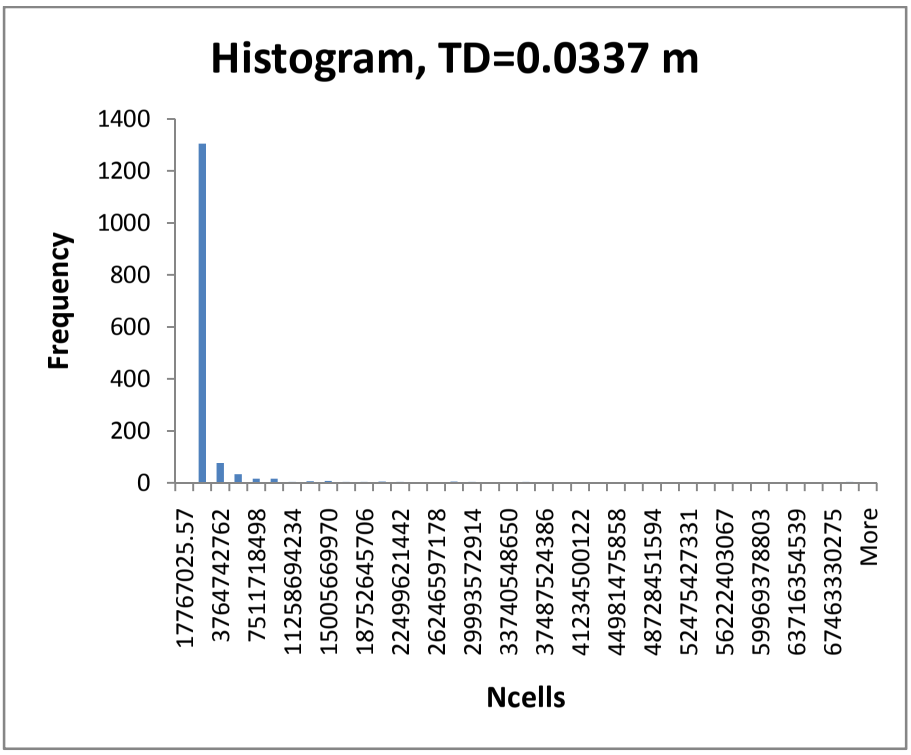

Figure 43: Histogram of N_{cells} with the tumor diameter of 0.0337m

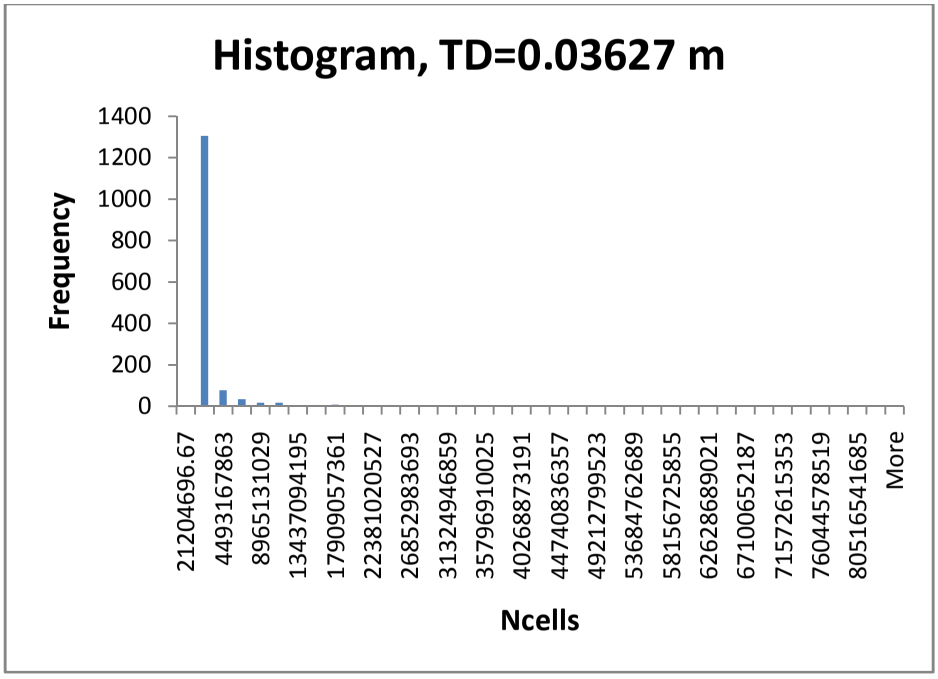

Figure 44: Histogram of N_{cells} with the tumor diameter of 0.03627 m

16. Appendix E – Scaleup Costs, FCI, and TCI

	Process step	Equipment	Scaleup capacity		Cost
Attaching mAb to CNT	Preparation of SWNT in PBS	Bead mills	15.27	L	$10,000.00
		Centrifuge	15.27	L	$104,602.72
	Addition of surfactants to SWNT	Mixer	0.61	L	$16.58
		Mixer	15.27	L	$16.66
		Microfilter	1.45	g	$36,919.50
		Mixer/storage	15.27	L	$16.66
	Preparation of antibody solution	Mixer	373.32	L	$18.71
		Mixer	373.32	L	$18.71
		Centrifuge	0.61	L	$4,184.11
Producing mAb	Equipment as a % of TCI				$27,487,352.45
		Total Delivered Equipment Cost:			$27,633,146.09

		Average multiplier	Amount
Direct costs:			
	Purchased equipment delivered	1	$27,633,146.09
	Purchased equipment installed	0.5	$13,816,573.04
	Instrumentation and controlls (installed)	0.35	$9,671,601.13
	Piping (installed)	0.03	$828,994.38
	Electrical systems (installed)	0.15	$4,144,971.91
	Buildings (including services)	0.45	$12,434,915.74
	Yard improvements	0.15	$4,144,971.91
	Service facilities (installed)	0.5	$13,816,573.04
	Total direct plant cost		$86,491,747.25
Indirect costs:			
	Engineering and supervision	0.25	$6,908,286.52
	Construction expenses	0.35	$9,671,601.13
	Contractor's fee	0.05	$1,381,657.30
	Contingency	0.1	$2,763,314.61
	Total indirect plant cost		$20,724,859.56
	FCI		$107,216,606.81
Working capital		0.74	$20,448,528.10
	TCI		$127,665,134.91

Source: Plant Design and Economics for Chemical Engineers, Peters, Timmerhaus, and West (2003).

17. Appendix F – Total Product Cost

Product:	Mab-SWNT conjugate	**Capacity, kg/batch:**	1.603743022
Operating time, h/yr:	8400	**batches per year:**	383.2798471
Capacity, kg/yr:	614.6823803	**FCI:**	$107,216,606.81

		Suggested factor	Rate or quantity per year	Cost per rate or quantity unit	Calculated values (for 2008)
Raw Materials					
	SWNT		0.716293768 kg/yr	500 /kg	$364.90
	Mab		613.9660866 kg/yr	0	$0.00
	1-pyrenebutanoyl succinimide		610.5484127 kg/yr	108.5 /kg	$68,487.21
	methanol		6105.484127 L/yr	2052 /200 L	$64,763.02
	PEG		610.5484127 kg/yr	134.6 /5 kg	$16,992.40
	PBS		31.77185975 L/yr	40 /2 L	$656.95
	Ammonium sulfate		294677.9746 kg/yr	775.4 /25 kg	$9,312,025.03
	Glycerol		8427.179672 kg/yr	59.7 /kg	$512,586.61
	Growth media		99121.85387 kg/yr	5 /kg	$514,631.91
	Na3 citrate		3644.185804 kg/yr	221.8 /10 kg	$82,351.73
	Phosphoric acid		4741996.778 kg/yr	69.2 /kg	$334,332,056.47
	Sodium chloride		251357.7158 kg/yr	267.5 /kg	$68,505,695.24
	Sodium hydroxide		31112.2363 kg/yr	103.2 /25 kg	$131,733.89
	Tris-HCl		3143.110256 kg/yr	788.9 /kg	$2,526,342.58
	Water		52198406.41 kg/yr	1.1 /1000 kg	$58,923.29
	Water for Injection		83219538.07 kg/yr	1.1 /1000 kg	$93,267.14
				Total	**$416,220,878.38**

	Suggested factor	Rate or quantity per year		Cost per rate or quantity unit	Calculated values (for 2008)
Operating labor		2800	hr/yr	25.86	$72,403.93
Operating supervision	0.15	of operating labor			$10,860.59
Utilities					
Water					
Cooling:		0			$0.00
Process:			m^3/yr	0.04	$0.00
Electricity			kWh	0.051	$0.00
Fuel		0			$0.00
Refrigeration		0			$0.00
Steam		0			$0.00
Waste treatment and disposal		0			$0.00
Maintenance and repairs	0.07	of FCI			$7,646,642.20
Operating supplies	0.15	of maintenance and repairs			$1,146,996.33
Laboratory charges	0.15	of operating labor			$10,860.59
Royalties	0.04	of TPC w/out depreciation			$0.00
Catalysts and solvents		0			$0.00
				Total variable production costs	$8,887,763.65
Taxes (property)	0.02	of FCI			$0.00
Financing (interest)	0	of FCI			$0.00
Insurance	0.01	of FCI			$1,092,377.46
Rent	0	of FCI			$0.00
Depreciation		5360830.341			$5,360,830.34
				Fixed Charges (w/out depriciation)	$1,092,377.46
				Plant overhead costs	$42,620,101.95
				Administrative costs	(inc. above)
				Distribution & marketing costs	(inc. above)
				Research and development	(inc. above)
				General Expenses	$42,620,101.95
				Total Product Cost	**$468,821,121.43**
				Total Product Cost/kg	**$763,594.49**
				Total Product Cost/g	**$763.59**

18. Appendix G – Net Present Worth

Total Capital Investment:	$127,665,134.91
Selling Price ($/g):	$1,527.19
Production Rate (kg/yr):	614.68
Selling Price Multiplier	2

	Year	Price ($/g)	Income from sales	Annual Product Cost	Cash Flow	NPV (with i = 10%)
1	2008	$1,527	$938,736,159	$487,573,966	$169,541,345	$154,128,495
2	2009	$1,538	$945,441,522	$507,076,925	$154,732,140	$127,877,802
3	2010	$1,549	$952,379,613	$527,360,002	$139,305,727	$104,662,455
4	2011	$1,561	$959,317,705	$548,454,402	$123,067,991	$84,057,094
5	2012	$1,572	$966,255,796	$570,392,578	$105,986,479	$65,809,265
6	2013	$1,583	$973,193,887	$593,208,281	$88,027,440	$49,689,195
7	2014	$1,595	$980,131,979	$616,936,612	$69,155,773	$35,487,846
8	2015	$1,606	$987,070,070	$641,614,077	$49,334,972	$23,015,129
9	2016	$1,617	$994,008,162	$667,278,640	$28,527,073	$12,098,264
10	2017	$1,628	$1,000,946,253	$693,969,786	$6,692,591	$2,580,284
					NPV	**$542,204,770**

19. Appendix H – Finite Difference Method Equations

Transient Heat Conduction

The energy balance of the transient heat conduction on a volume element during a time Δt can be shown as[40]

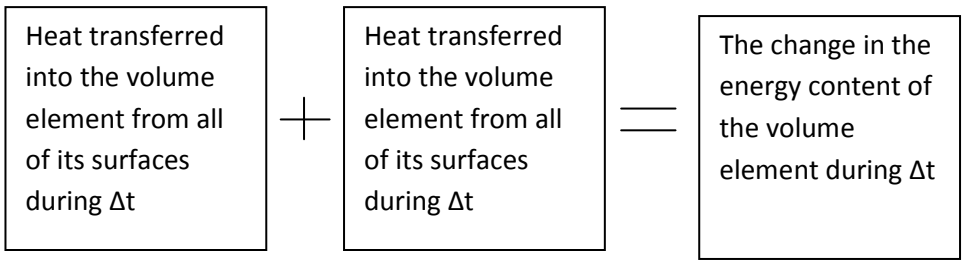

Or

$$\Delta t \times \sum_{Surface} \dot{Q} + \Delta t \times \dot{E_{gen}} = \Delta E_{element} \qquad \textbf{Equation 39}$$

where $\Delta E_{element} = mc_p\Delta t = \rho \forall_{element} c_p \Delta T/\Delta t$. Equation 30 can be expressed in terms of Δt as

$$\sum_{Surface} \dot{Q} + \dot{E_{gen}} = \frac{\Delta E_{element}}{\Delta t} = \rho \forall_{\text{element}} c_p \frac{\Delta T}{\Delta t} \qquad \textbf{Equation 40}$$

Equation 32 can be expressed for any node *m* at times *i* and *i+1* as

$$\sum_{Surface} \dot{Q} + \dot{E_{gen}} = \rho \forall_{\text{element}} c_p \frac{T_m^{i+1} - T_m^i}{\Delta t} \qquad \textbf{Equation 41}$$

where T_m^i and T_m^{i+1} are the temperatures of nodes m at times $t_i = i\Delta t$ and $t_{i+1} = (i+1)\Delta t$, respectively. The term $\frac{T_m^{i+1} - T_m^i}{\Delta t}$ denotes the temperature change of the node during the time interval Δt between the time steps *i* and *i*+1. As mentioned above, the explicit method is used and the general form of the equation is

$$\sum_{Surface} \dot{Q^i} + \dot{E_{gen}^i} = \rho \forall_{\text{element}} c_p \frac{T_m^{i+1} - T_m^i}{\Delta t} \qquad \textbf{Equation 42}$$

Energy Balance on Each Type of Node

The only heat transfer through the control surface of the center node is by conduction from its surrounding node. This is expressed as

$$\dot{Q} = k(4\pi\left(\frac{\Delta r}{2}\right)^2)\frac{T_1^i - T_0^i}{\Delta r} \qquad \textbf{Equation 43}$$

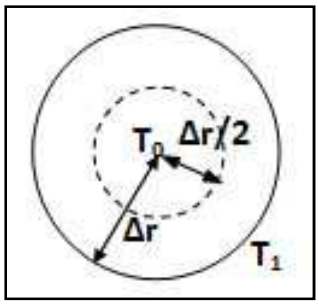

Figure 47: Center node

E_{gen}^i is the heat generation within the control volume of node due to the NIR radiation expressed by

$$E_{gen}^i = g\left(\frac{4}{3}\pi\right)\left(\frac{\Delta r}{2}\right)^3 \qquad \textbf{Equation 44}$$

where g is the volumetric heat generation rate of $6.156*10^6$ W/m^3. The value g is calculated based on the assumption that the radiation heat flux comes from the NIR radiation. The radiation heat flux was absorbed by the half of the surface area of the tumor sphere. Therefore the heat absorbed by the sphere due to NIR radiation is equal to the heat generated within the total volume of the sphere expressed as

$$\dot{q_{rad}}A_{rad} = gV_{total} \qquad \textbf{Equation 45}$$

where q_{rad} is the NIR heat flux 8000 W/m^2, A_{rad} is the half surface area of the sphere, and V_{total} is the total volume of the sphere.

The right side of Equation 36 in the center node can be expressed as

$$\rho \vee_{element} c_p \frac{T_m^{i+1} - T_m^i}{\Delta t} = \rho \vee_{center} c_p \frac{T_0^{i+1} - T_0^i}{\Delta r} \qquad \textbf{Equation 46}$$

Adding the heat transfer rate into the control volume and heat generated within the control volume and setting these terms equal to the above term yields the center temperature finite difference equation.

$$T_0^{i+1} = \frac{4\pi k \Delta t}{\rho V c_p}\left(\frac{\Delta r}{2}\right)^2 \frac{T_1^i}{\Delta r} + \left(1 - \frac{4\pi k \Delta t}{\rho V c_p}\left(\frac{\Delta r}{2}\right)^2\right) T_0^i + T_0^i \qquad \textbf{Equation 47}$$

The Interior Nodes

The interior nodes include all the nodes between the center nodes and the outside surface of the sphere. The only heat transfer into the interior nodes is by conduction between adjacent nodes.

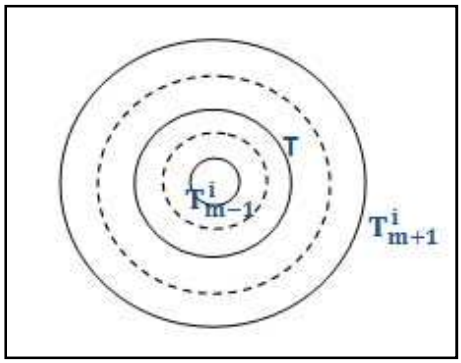

Figure 48: Interior node

The heat transfer rates by conduction into the control volume from the nodes on either side of an interior node are given by

$$\dot{Q}_{inside} = 4\pi k\left(r - \frac{\Delta r}{2}\right)^2 \frac{T^i_{m-1} - T^i_m}{\Delta r} \qquad \textbf{Equation 48}$$

$$\dot{Q}_{outside} = 4\pi k\left(r + \frac{\Delta r}{2}\right)^2 \frac{T^i_{m+1} - T^i_m}{\Delta r} \qquad \textbf{Equation 49}$$

The rate of heat generation in the control volume is given by

$$E^i_{gen} = g\left(\frac{4}{3}\pi\right)\left(\left(r + \frac{\Delta r}{2}\right)^3 - \left(r - \frac{\Delta r}{2}\right)^3\right) \qquad \textbf{Equation 50}$$

Therefore the formulated finite difference equation for the interior nodes is given by

$$T_m^{i+1} = \frac{4\pi k \Delta t}{\rho V c_p \Delta r}\left(\left(r - \frac{\Delta r}{2}\right)^2 (T_{m-1}^i - T_m^i) + \left(r + \frac{\Delta r}{2}\right)^2 (T_{m+1}^i - T_m^i)\right) + \frac{g\Delta t}{\rho c_p} + T_m^i \quad \textbf{Equation 51}$$

The Surface Node

The surface node experiences the heat transfer by conduction through the adjacent interior node and convection from the medium around the sphere. The heat transfer rate of conduction and convection is given by

$$\text{Conduction: } \dot{Q} = 4\pi k \left(r - \frac{\Delta r}{2}\right)^2 \frac{T_{m-1}^i - T_m^i}{\Delta r} \quad \textbf{Equation 52}$$

$$\text{Convection: } \dot{Q} = h(4\pi r^2)\left(T_\infty - T_m^i\right) \quad \textbf{Equation 53}$$

The heat transfer coefficient h is calculated by using a natural convection correlation. The Rayleigh number is given by

$$Ra = \frac{g\beta(T_S - T_\infty)D^3}{\nu^2} Pr \quad \textbf{Equation 54}$$

where g is the acceleration to gravity, β is the volumetric expansion rate, T_s is the temperature of the surface, T_∞ is the ambient temperature, D is the sphere diameter, ν is the kinematic viscosity of water since it is assumed that the medium is consisted with water, and Pr is the Prandtl number.

The Nusselt number correlation is now can be calculated by

$$Nu = 2 + \frac{0.589 Ra^{0.25}}{\left(1 + \left(\frac{0.469}{\Pr}\right)^{\frac{9}{16}}\right)^{4/9}} = \frac{hD}{k} \quad \textbf{Equation 55}$$

where k is the conductivity of water. The heat transfer coefficient can be determined once the Nusselt number is calculated.

The energy generation rate in the control volume of the surface node is given by

$$E_{gen}^{i} = g\left(\frac{4}{3}\pi\right)\left(R^3 - \left(R - \frac{\Delta r}{2}\right)^3\right) \qquad \textbf{Equation 56}$$

The formulated finite differences equation is given by

$$T_m^{i+1} = \frac{4\pi k\Delta t}{\rho V c_p \Delta r}\left(r - \frac{\Delta r}{2}\right)^2 (T_{m-1}^{i} + T_m^{i}) + \frac{4\pi r^2 h\Delta t}{\rho V c_p}\left(T_m^{i} + T_\infty\right)^2 + \frac{g\Delta t}{\rho c_p} + T_m^{i}$$

Stability Criterion

As mentioned above, the stability criterion should be considered in order to have the convergent solution in the explicit method in the simulation. The stability criterion requires that the following inequalities be satisfied.

For center node: $1 - \frac{4\pi k\Delta t}{\rho V c_p \Delta r}\left(\frac{\Delta r}{2}\right)^2 > 0$

Interior nodes: $1 - \frac{4\pi k\Delta t}{\rho V c_p \Delta r}\left(\left(r - \frac{\Delta r}{2}\right)^2 + \left(r + \frac{\Delta r}{2}\right)^2\right) > 0$

Surface node: $1 - \frac{4\pi k\Delta t}{\rho V c_p \Delta r}\left(R - \frac{\Delta r}{2}\right)^2 + \frac{4\pi R^2 h\Delta t}{\rho V c_p} > 0$

The convenient time step was chosen and the stability criterion was checked to ensure that the solution was convergent.